

# Extreme $\delta^{18}\text{O}$ signatures in zircon from the Saglek Block document reworking of mature supracrustal rocks as early as 3.5 Ga;

Vezinet et al.,

## Supplementary Material

<b>1</b>	<b>The Hebron Fjord outcrop and the meta-tonalite LA9-01.....</b>	<b>2</b>
<b>2</b>	<b>Laser-ablation split stream (LASS) analyses .....</b>	<b>3</b>
2.1	Metadata of the laser-ablation split-stream U–Th–Pb/Lu–Yb–Hf analyses .....	3
2.2	Iolite data reduction.....	5
2.3	Identification of common-Pb during zircon U–Pb analyses.....	5
2.4	Zircon reference material.....	7
2.5	U–Pb Tera-Wasserburg diagram.....	14
<b>3</b>	<b>Ion probe zircon oxygen-isotope measurements .....</b>	<b>15</b>
<b>4</b>	<b>Zircon trace element analyses .....</b>	<b>17</b>
4.1	Method for trace element analyses by LA-ICP-MS.....	17
4.2	Chemical screening .....	17
4.1	Trace element composition of optically disturbed zircon domains .....	18
<b>5</b>	<b>The role of the <math>^{176}\text{Lu}/^{177}\text{Hf}</math> ratio in the evolution of the Hf signature .....</b>	<b>19</b>
<b>6</b>	<b>Compiled dataset of zircon <math>\delta^{18}\text{O}</math> value.....</b>	<b>21</b>
<b>7</b>	<b>Uncertainty propagation workflow .....</b>	<b>22</b>
7.1	Uncertainty on the U–Th–Pb isotope ratios and dates .....	22
7.2	Uncertainty on the $(^{176}\text{Hf}/^{177}\text{Hf})_{\text{initial}}$ ratio.....	22
7.3	Uncertainty on the $\epsilon\text{Hf}$ ratio .....	23
<b>8</b>	<b>Methodology for the determination of whole-rock major- and trace-elements composition .....</b>	<b>23</b>
	<b>References .....</b>	<b>24</b>

## 1 The Hebron Fjord outcrop and the meta-tonalite LA9-01

The rock specimen LA9-01 was sampled on the shore of the Hebron Bight (see Figure 1 of the main manuscript) at: N58.20639–W62.59940. This exposure, represented in the Figure 1 here below, is made of strongly deformed felsic phaneritic material. Both metatexite and diatexite are encountered at outcrop scale (see also Figure 1 of the main manuscript). Boundins of mafic to ultramafic material are found embedded, and deformed, in the main felsic component. Layers of Fe-rich material (likely of sedimentary origin) are also encountered within the deformed felsic complex. Altogether, the Hebron Bight outcrop matches the features of an Archean grey gneiss complex (as defined in [Moyen, 2011](#)). The highly deformed aspect of all lithologies exposed in the Hebron Bight, plus the presence of metatexite and diatexite, strongly suggest metamorphic overprinting after emplacement of these lithologies.



Figure 1: Exposure on the Hebron Bight (Saglek Block)



Figure 2: Photography of the hand-specimen LA9-01.

Figure 2 shows the hand-specimen made of millimetre-sized grains demonstrating the phaneritic nature of the rock sample. Both the outcrop and the hand-specimen show textural features encountered in high-grade terranes, i.e. gradational transition between metatexites toward diatexites (see [Brown, 1973](#) for definition and meaning of these terms).

The mineral assemblage of the meta-tonalite LA9-01 consists of: Pl + Qz + Bt + Zrn + Ap + Spn (abbreviation after [Whitney and Evans, 2010](#)). Isotope study of titanite and apatite grains from rocks of the Saglek region yield Neoarchean and Paleoproterozoic ages ([Baadsgaard et al., 1979](#); [Kusiak et al., 2018](#)). Experimental investigations have suggested that rocks of felsic chemical composition crystallise zircon prior to apatite and titanite such that appearance of the latter two should not alter the trace element content of the zircon.

## 2 Laser-ablation split stream (LASS) analyses<sup>1</sup>

### 2.1 Metadata of the laser-ablation split-stream U–Th–Pb/Lu–Yb–Hf analyses

Table 1 below shows the main analytical parameters that have been used to conduct the concurrent U–Th–Pb and Lu–Yb–Hf isotope measurements using laser-ablation split stream (LASS) protocol (see also Fisher *et al.*, 2017). The metadata reporting of U–Th–Pb analyses follows the recommendations of Horstwood *et al.* (2016) and metadata reporting Lu–Yb–Hf analyses follows the recommendations of Fisher *et al.* (2014). Some of these are further detailed in the following.

**Table 1: Metadata for the laser-ablation split-stream analyses performed during this study**

<b>Laboratory &amp; Sample Preparation</b>	
Laboratory name	Arctic Resource Lab, University of Alberta (Canada)
Sample type/mineral	Complex zircon grains (magmatic + metamorphic domains)
Sample preparation	Conventional mineral separation, polished 1 inch resin mount,
Imaging	CL & BSE (Gemini supra 55 VP Zeiss; EVO MA15 Zeiss; JEOL JSM-5910 LV)
<b>Laser ablation system</b>	
Make, Model & type	RESolution ArF excimer
Ablation cell	Laurin Technic S-155
Laser wavelength	193 nm
Pulse width	4 ns
Fluence	3 J.cm <sup>-2</sup> for October, 2017 analytical sequences and <i>ca.</i> 6.5 J.cm <sup>-2</sup> (120 mJ, 44% transmission) for March, 2018 analytical sequences.
Repetition rate	8 Hz
Ablation/Washout duration	45 secs / 45 secs
Ablation rate	0.125 $\mu\text{m.pulse}^{-1}$ with the <i>ca.</i> 6.5 J.cm <sup>-2</sup> setting
Spot diameter nominal/actual	33 $\mu\text{m}$ / 44 $\mu\text{m}$
Sampling mode / pattern	Static spot ablation
Carrier gas	100% He in the cell, Ar and N <sub>2</sub> make-up gas combined using a Y-piece 50% along the sample transport line to the torch.
Cell carrier gas flow	0.8- 0.9 l.min <sup>-1</sup>
<b>ICP-MS Instruments</b>	
<b>U–Th–Pb measurements</b>	
Make, Model & type	Thermo Fisher Scientific, Element XR, SC-SF-ICP-MS
Sample introduction	Ablation aerosol introduced through Tygon tubing
RF power	1360W
Make-up gas flow (l/min)	Total gas is made of ~1.6 l.min <sup>-1</sup> of Ar, 0.8-0.9 l.min <sup>-1</sup> of He and 12-14 ml.min <sup>-1</sup> of N <sub>2</sub> . This total gas is divided between both ICP-MS at a ~ 50-50 rate.
Detection system	202, 208, 232 in triple mode. 206 and 238 in analogue mode. 204 and 207 in counting mode 235 is calculated using canonical value. No Faraday cup used.
Masses measured	202, 204, 206, 207, 208, 232, 238

<sup>1</sup> Sections 2.1, 2.2 and 2.3 are identical to those reported in the Electronic Supplementary Material of Vezinet *et al.* (2018).

**Table 1: (continuation)**

ICP-MS Instruments (continuation)									
U–Th–Pb measurements (continuation)									
Integration time per peak/ dwell times	30 ms on 202, 204, 208 and 232; 60 ms on 206, 207 and 238								
Total integration time	300 ms for each output datapoint								
IC Dead time	20 ns								
ICP-MS Instruments									
Lu–Yb–Hf measurements									
Make, Model & type	Thermo Fisher Scientific, Neptune Plus, MC-SF-ICP-MS								
Sample introduction	Ablation aerosol introduced tygon tubing. Ni-Jet Sample cone and X-Skimmer cone.								
RF power	1300W								
Make-up gas flow (l/min)	Total gas is made of ~1.6 l.min <sup>-1</sup> of Ar, 0.8-0.9 l.min <sup>-1</sup> of He and 12-14 ml.min <sup>-1</sup> of N <sub>2</sub> . This total gas is divided between both ICP-MS at a ~ 50-50 rate.								
Detection system	Static Faraday (attached to 10 <sup>11</sup> Ω amplifier) measurement								
Masses measured	172, 173, 175, 176, 177, 178, 179, 180, 181								
Total integration time per output datapoint	1.049 secs								
Cup configuration	L4	L3	L2	L1	Axial	H1	H2	H3	H4
	172	173	175	176	177	178	179	180	181
Data Processing									
Gas blank	30 second on-peak zero subtracted both for U-Pb and Lu-Hf measurements								
Calibration strategy	LH94-15 used as primary reference material, Plešovice, GJ-1, 91500 & FC-1 used as secondaries/validation materials.								
Reference Material info	LH94-15 (Ashton <i>et al.</i> , 1999; Simonetti <i>et al.</i> , 2005)								
	GJ-1 (Jackson <i>et al.</i> , 2004; Morel <i>et al.</i> , 2008)								
	Plešovice (Sláma <i>et al.</i> , 2008)								
	Mud Tank (Horstwood <i>et al.</i> , 2016)								
Data processing package used / Correction for LIEF	MUN-zircon (Fisher <i>et al.</i> , 2011)								
	Iolite software package (Paton <i>et al.</i> , 2010; Paton <i>et al.</i> , 2011; Fisher <i>et al.</i> , 2017) using the following DRS: “ <i>U_Pb Geochron 4</i> ” for U–Th–Pb isotope analyses and “ <i>Hf_Alberta</i> ” for Lu–Yb–Hf isotope. LIEF correction assumes matrix match between reference material and samples.								
	Standard-sample bracketing with <sup>207</sup> Pb/ <sup>206</sup> Pb and <sup>206</sup> Pb/ <sup>238</sup> U normalized to primary reference material.								
	No common-Pb correction applied to the data								
Common-Pb correction, composition and uncertainty	No common-Pb correction applied to the data								
Yb mass bias coefficient (β <sup>Yb</sup> )	Calculated using <sup>173</sup> Yb/ <sup>172</sup> Yb invariant ratio and the exponential law of Russell <i>et al.</i> (1978).								
Yb interference	Calculated with <sup>176</sup> Yb/ <sup>173</sup> Yb ratio, the Yb-mass bias coefficient (β <sup>Yb</sup> ) and the exponential law of Russell <i>et al.</i> (1978). Daily adjusted.								
Lu interference	Calculated with <sup>176</sup> Lu/ <sup>175</sup> Lu ratio, the Yb-mass bias coefficient (β <sup>Yb</sup> ) and the exponential law of Russell <i>et al.</i> (1978). Daily adjusted.								
Uncertainty level & propagation	Ages are quoted at a coverage factor of 2, absolute. Propagation is by quadratic addition. Reproducibility and age uncertainty of reference material and common-Pb composition uncertainty are propagated where appropriate.								
Quality control / Validation	Results of LASS analyses on validation zircon reference material are reported in Figure 4 and Figure 5 for the U–Th–Pb isotope system and Figure 6 to Figure 8 for the Lu–Yb–Hf isotope system.								



## 2.2 Iolite data reduction

LASS analyses were processed offline using the Data Reduction Scheme (DRS) supplied by Iolite v3 software (Paton *et al.*, 2010; Paton *et al.*, 2011). Isotope measurements from both the SC-SF-ICP-MS (U–Th–Pb isotope measurements) and the MC-SF-ICP-MS (Lu–Yb–Hf isotope measurements) were processed simultaneously through the “Run in Multiple DRS mode” option of the Iolite v3 software. This option implies that for each LASS analysis the integration time of the U–Th–Pb isotope analysis and the integration time Lu–Yb–Hf isotope analysis are identical (i.e. begins at the same time  $t$ , and lasts the same time). Moreover, as demonstrated in Figure 3, the integration time is manually determined for each single analysis in order to best represent the area of the grain selected prior LASS analysis.

## 2.3 Identification of common-Pb during zircon U–Pb analyses

In addition to the masses 206, 207 and 208, we also measured the intensity on mass 204 to constrain the amount of common lead during the U–Pb analyses. To limit mercury (Hg) contamination and isobaric interferences in lead measurement, we used 3 Hg traps (VICI® Metronics Hg trap) positioned on the Ar line, the He line and the  $\text{N}_2$  line. As the mass resolution power used in this study ( $M/\Delta M=300$ ) is not sufficient to separate  $^{204}\text{Pb}$  ( $m=203.973044$ ) and  $^{204}\text{Hg}$  ( $m=203.973494$ ) – that requires a  $M/\Delta M$  of *ca.* 408,000 – the signal obtained during scanning the 204-mass represents the combination of both isotopes. The potential contamination that would persist after the Hg-trapping step was thus quantified measuring mass 202, which is an interference-free mass of the  $^{202}\text{Hg}$ . Using the measured  $^{202}\text{Hg}$  value and the natural ratio of  $^{202}\text{Hg}/^{204}\text{Hg}$  ( $=29.74/6.82$ ), we calculated the proportion of the 204-mass signal attributable to  $^{204}\text{Hg}$  and hence the 204-mass signal attributable to  $^{204}\text{Pb}$ . The  $^{204}\text{Pb}$  value was then used to calculate the  $^{206}\text{Pb}/^{204}\text{Pb}$  ratio and, with reference to the model values of Stacey and Kramers (1975), to yield the  $f^{206}\text{Pb}_c$  reported in the Supplementary Table using the following equation:

$$f^{206}\text{Pb}_c(\%) = \frac{(^{206}\text{Pb}/^{204}\text{Pb})_{\text{Stacey \& Kramers, 1975}}}{(^{206}\text{Pb}/^{204}\text{Pb})_{\text{measured}}} \cdot 100$$

Using these parameters the  $(^{206}\text{Pb}/^{204}\text{Pb})_{\text{measured}}$  ratio must then be above 1054.4 for a 4 Ga-old zircon grain and above 1408.8 for a 2.5 Ga-old zircon grain to yield a  $f^{206}\text{Pb}_c$  value below 0.1% (which is the threshold used in this study).

We emphasise that, no common-Pb correction was necessary for the U–Pb data documented in the Supplementary Data table. When the  $f^{206}\text{Pb}_c$  was above the 0.1% threshold, the analysis was disregarded.

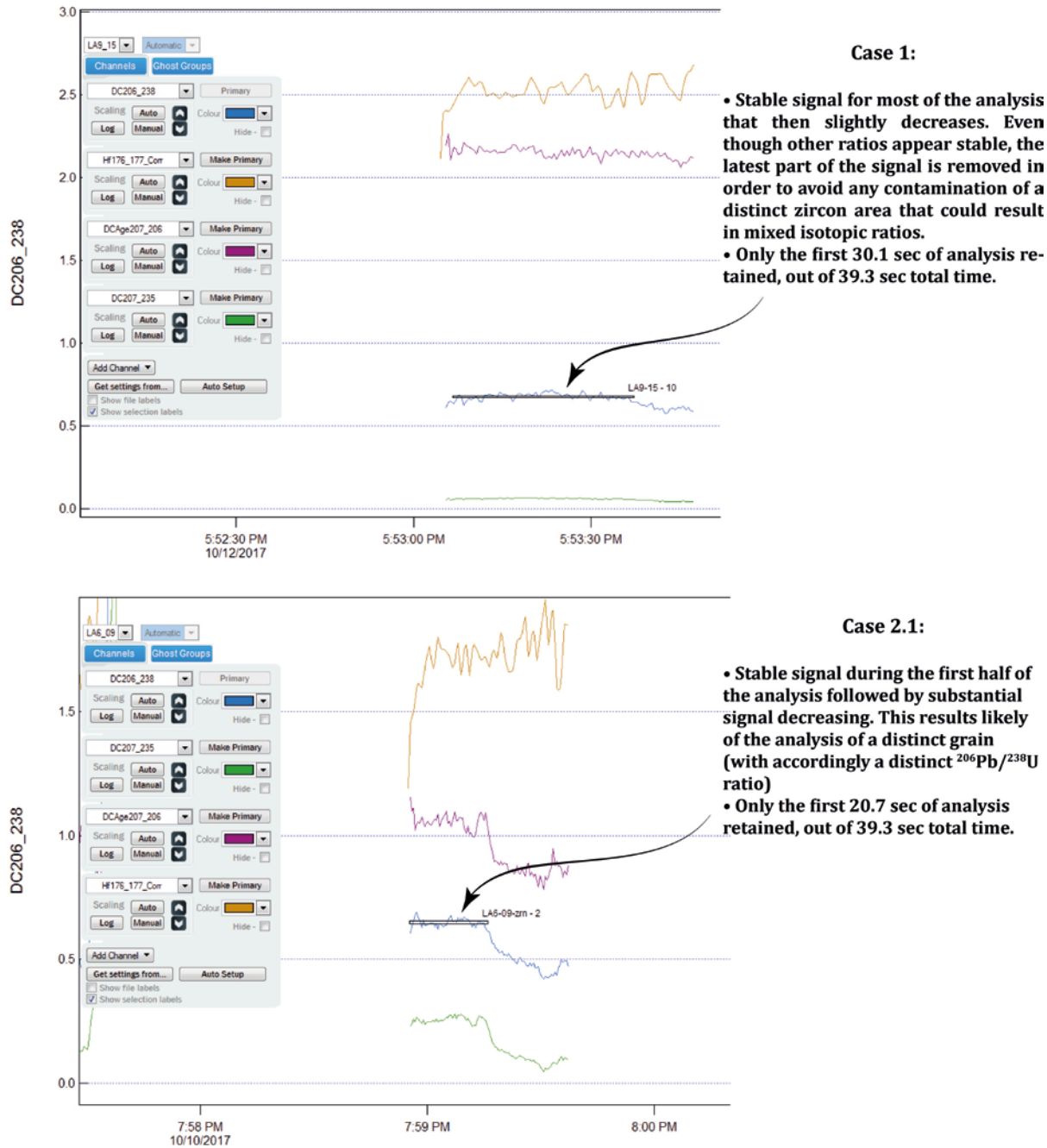


**Figure 3:** Time-resolved diagram obtained in the course of zircon LASS analysis data reduction during this study. These diagrams are drawn from the Iolite Main Windows. The X-axis represents the time, the Y-axis represents the intensity of the selected wave. The horizontal black stroke rectangle represents the selected integration time. On every image, the grey panel located on the left reports the name of the displayed waves. DC206\_208 = Down-hole Corrected  $^{206}\text{Pb}/^{238}\text{U}$  isotopic ratio; DC207\_235 = Down-hole Corrected  $^{207}\text{Pb}/^{235}\text{U}$  ratio; DCAge207\_206 = Down-hole Corrected  $^{207}\text{Pb}/^{206}\text{Pb}$  isotopic age; Hf176\_177\_corr =  $^{176}\text{Hf}/^{176}\text{Hf}$  isotopic ratio corrected from mass bias fractionation. On every diagram, DC206\_208 is the selected wave.

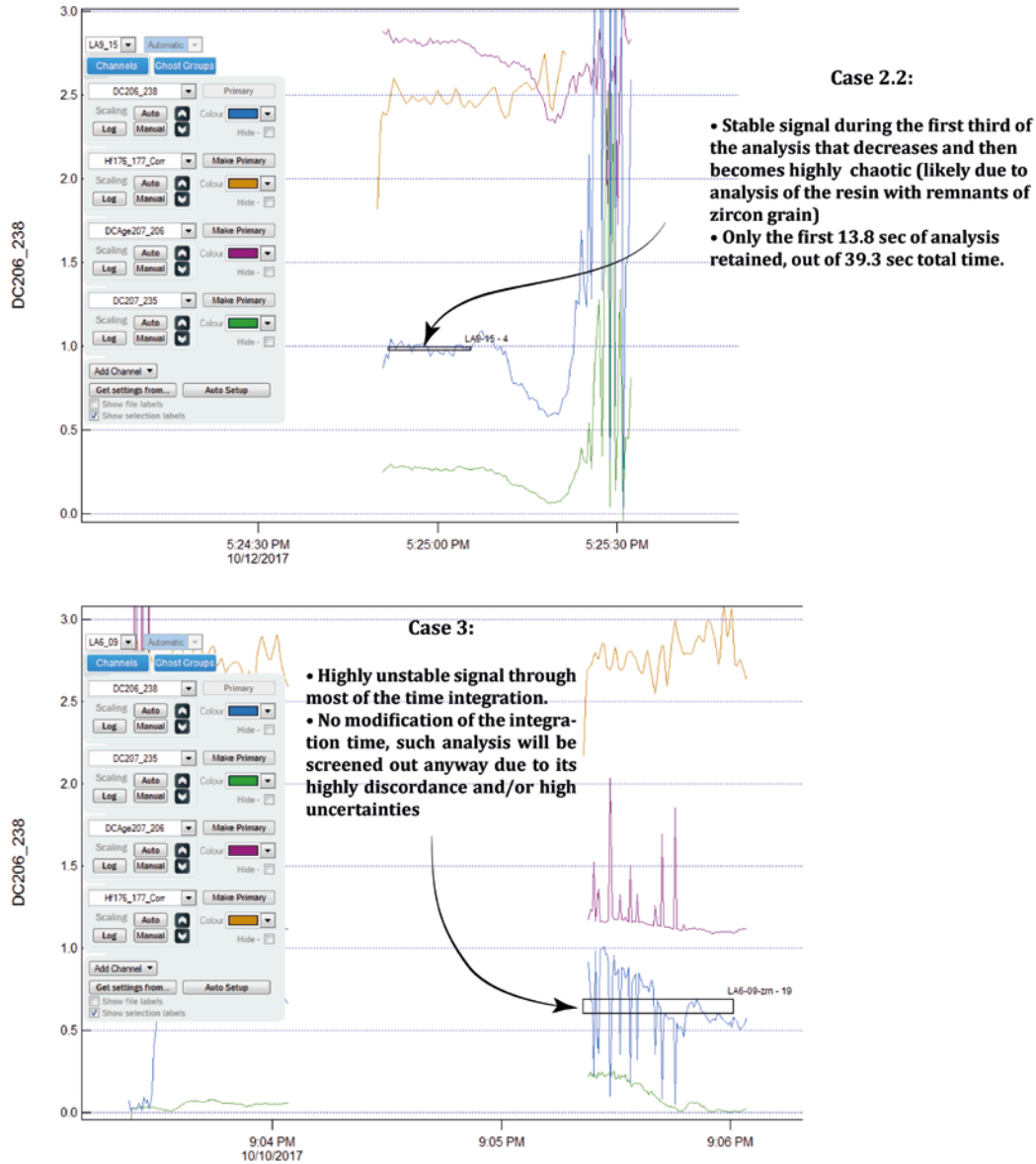


Figure 3: (continuation)

## 2.4 Zircon reference material

### 2.4.1 U–Pb weighted mean

During this study, zircon LH94-15 (Simonetti *et al.*, 2005) was used as primary (calibration) reference material for the U–Th–Pb isotope analyses. Three secondary (validation) reference materials were used in order to validate the primary correction: zircon GJ-1, Plešovice and Mud Tank (see Jackson *et al.*, 2004; Sláma *et al.*, 2008; and Horstwood *et al.*, 2016 respectively). Figure 4 reports the  $^{207}\text{Pb}/^{206}\text{Pb}$  dates of individual analyses as well as the associated weighted mean of validation and calibration zircon

reference material. The weighted mean dates displayed in each sub-panel of Figure 4 refer to the whole sample population (all reference material analyses).

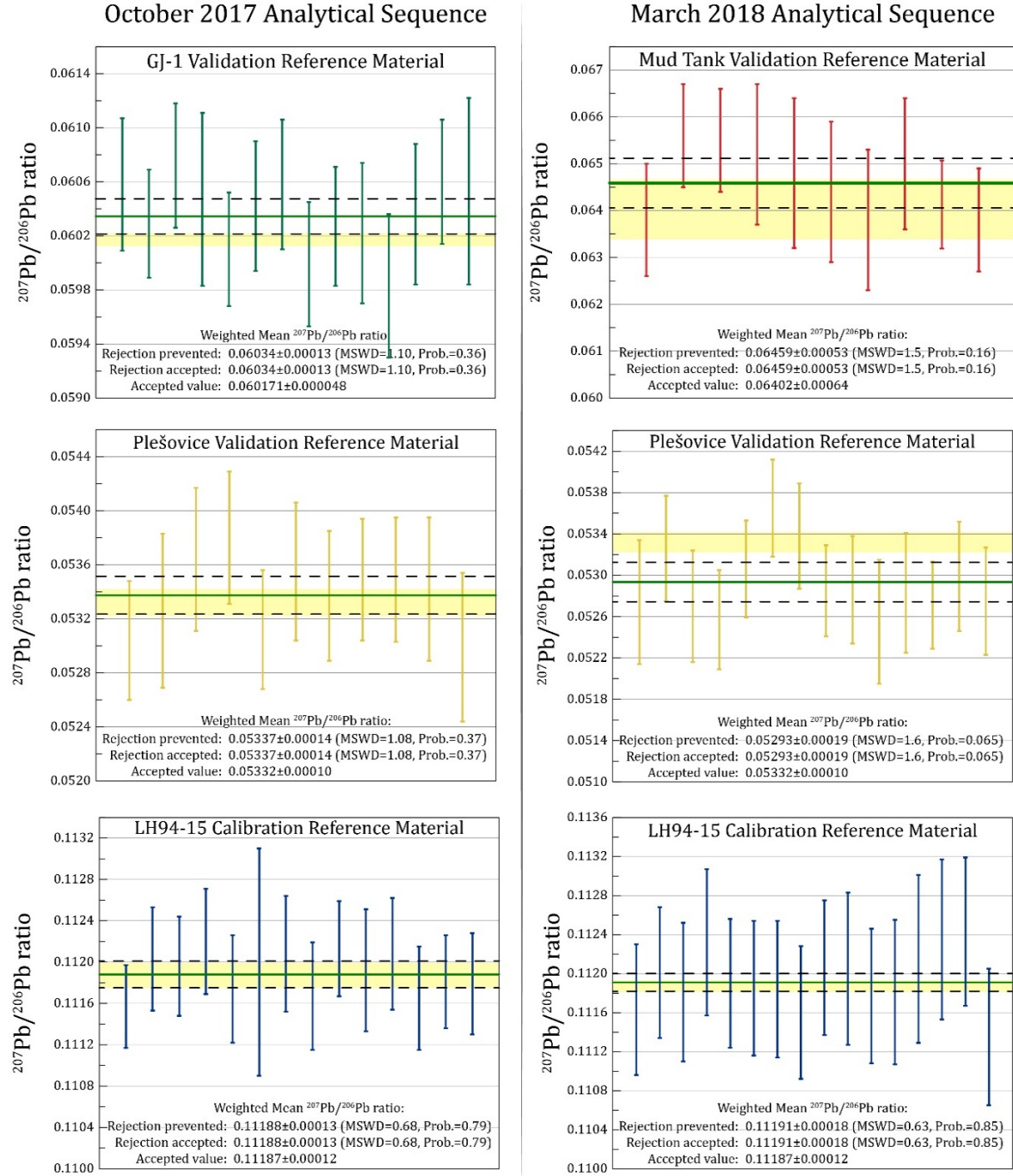


**Figure 4:**  $^{207}\text{Pb}/^{206}\text{Pb}$  weighted mean values relative to zircon reference material used in this contribution throughout the two analytical sequences. Vertical bars are individual analyses with absolute propagated 2 S.E. length. Colour code of the vertical bars is a function of the zircon reference material. Green horizontal bar represents the value of the weighted average (in the *rejection accepted* case), dotted horizontal lines represent the absolute 2 S.E. of the weighted mean. Yellow area represents the value and absolute 2 S.E. uncertainty of the accepted value. The weighted average of the calibration material (LH94-15) is displayed to reflect differences between each sequence of analyses and to demonstrate the good consistency throughout the course of a single sequence of analyses. The isotopic compositions of GJ-1, Mud Tank,

Plešovice and LH94-15 zircon reference material are after Morel *et al.* (2008), Horstwood *et al.* (2016), Sláma *et al.* (2008) and Simonetti *et al.* (2005) respectively. Diagrams produced using the Isoplot Add-In in Excel (Ludwig, 2003; 2012).

The  $^{207}\text{Pb}/^{206}\text{Pb}$  weighted means obtained after measurements of GJ-1, Mud Tank and Plešovice zircon validation materials are in agreement with reference values (yellow bands in Figure 4) obtained through ID-TIMS measurements reported in Morel *et al.* (2008), Horstwood *et al.* (2016) and Sláma *et al.* (2008).

## 2.4.2 Concordia diagrams

Figure 5 displays the Concordia diagrams for each sequence of analyses of the GJ-1, Plešovice, and Mud Tank zircon validation material. There is a good consistency between within-sequence analyses for the sequence ran during this work.

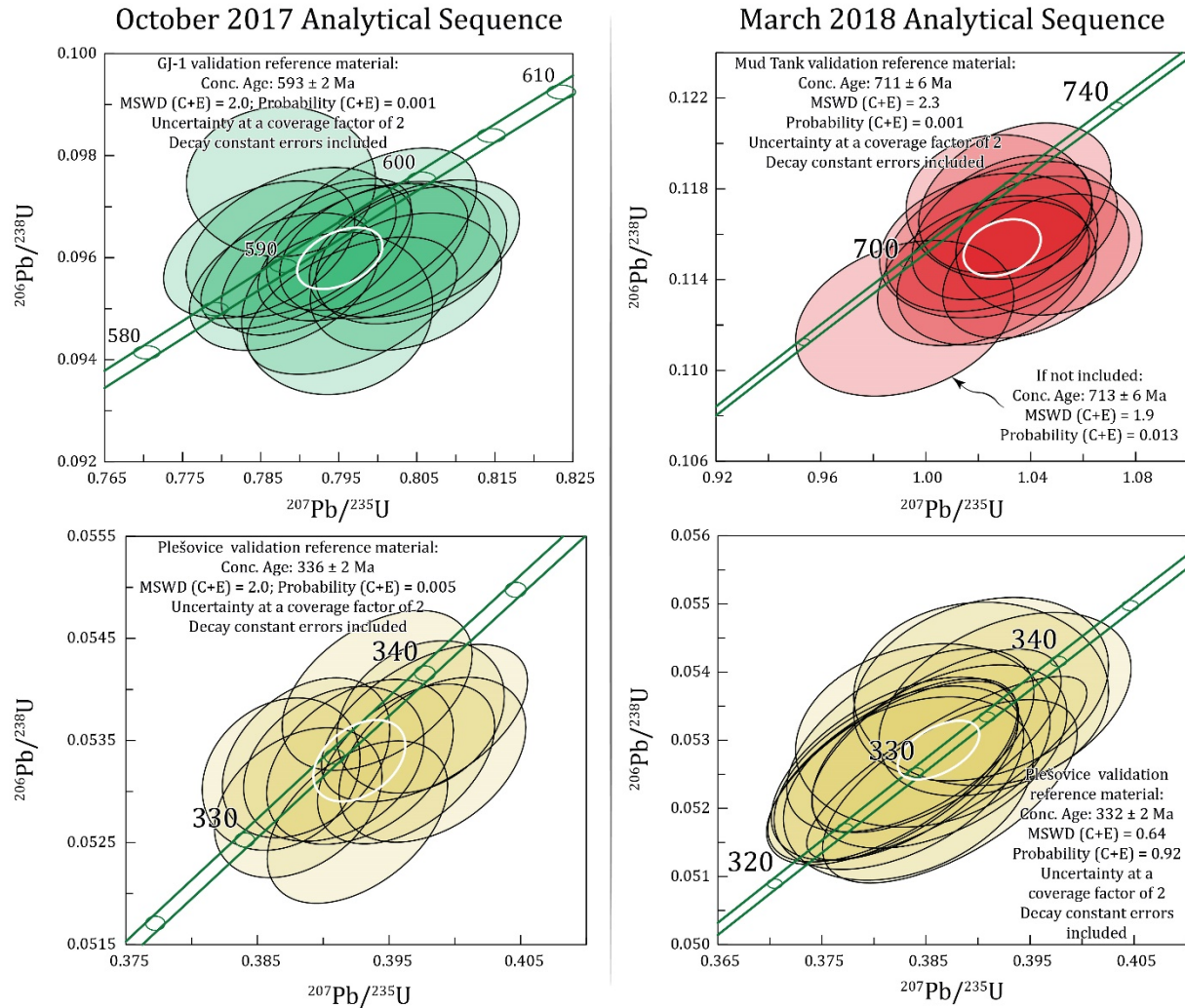


**Figure 5: Concordia diagrams for the GJ-1, Mud Tank and Plešovice zircon validation material. Each diagram represents an independent sequence of analyses. Colour code is similar to weighted average diagrams displayed in Figure 4. See text for details. Diagrams produced using the Isoplot Add-In in Excel (Ludwig, 2003; 2012).**



### 2.4.3 Correction of the isobaric interference from both $^{176}\text{Yb}$ and $^{176}\text{Lu}$ on $^{176}\text{Hf}$

The determination of the Yb-mass bias factor ( $\beta^{Yb}$ ) is achieved through the peak-stripping method, i.e. measurement of two interference-free isotope of Yb (Woodhead *et al.*, 2004; Fisher *et al.*, 2011). In this study, the invariant ratio measured is  $^{172}\text{Yb}/^{173}\text{Yb}$ . The value of the mass bias factor ( $\beta^{Yb}$ ) is then calculated following the exponential law introduced by Russell *et al.* (1978). Diagrams in Figure 6 show the constant  $^{176}\text{Hf}/^{177}\text{Hf}$  ratio despite large variation in the  $^{176}\text{Yb}/^{177}\text{Hf}$  ratio that reflects accurate correction of  $^{176}\text{Yb}$  interference on  $^{176}\text{Hf}$ . Finally, interference of  $^{176}\text{Lu}$  on  $^{176}\text{Hf}$  is handled via the same method.

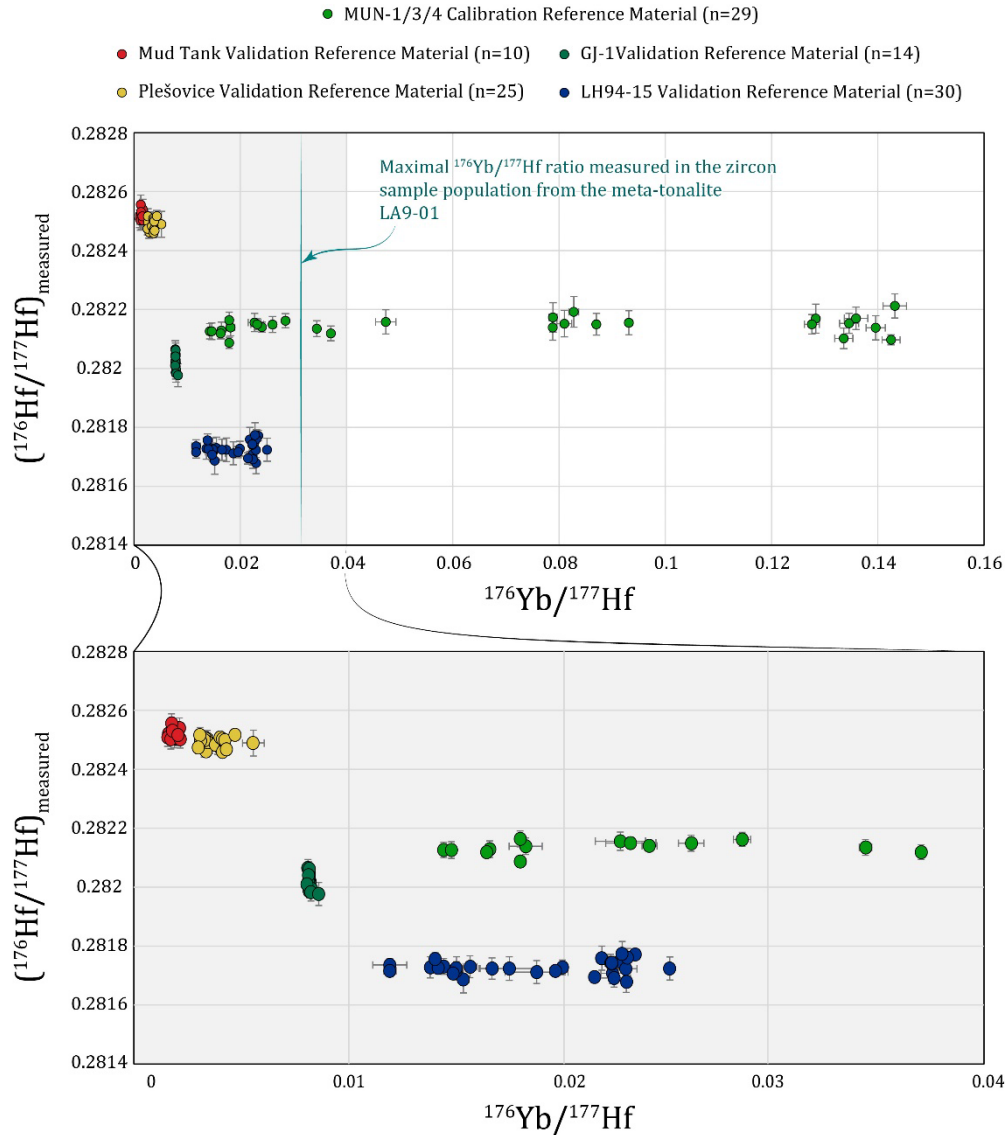


**Figure 6:**  $^{176}\text{Hf}/^{177}\text{Hf}$  ratio versus  $^{176}\text{Yb}/^{177}\text{Hf}$  ratio of individual analyses performed on zircon reference material MUN-1, MUN-4, GJ-1, Plešovice, Mud Tank and LH94-15. Uncertainty bars are absolute internal 2 S.E. The panel B is a zoom-in onto the grey area of the panel A.

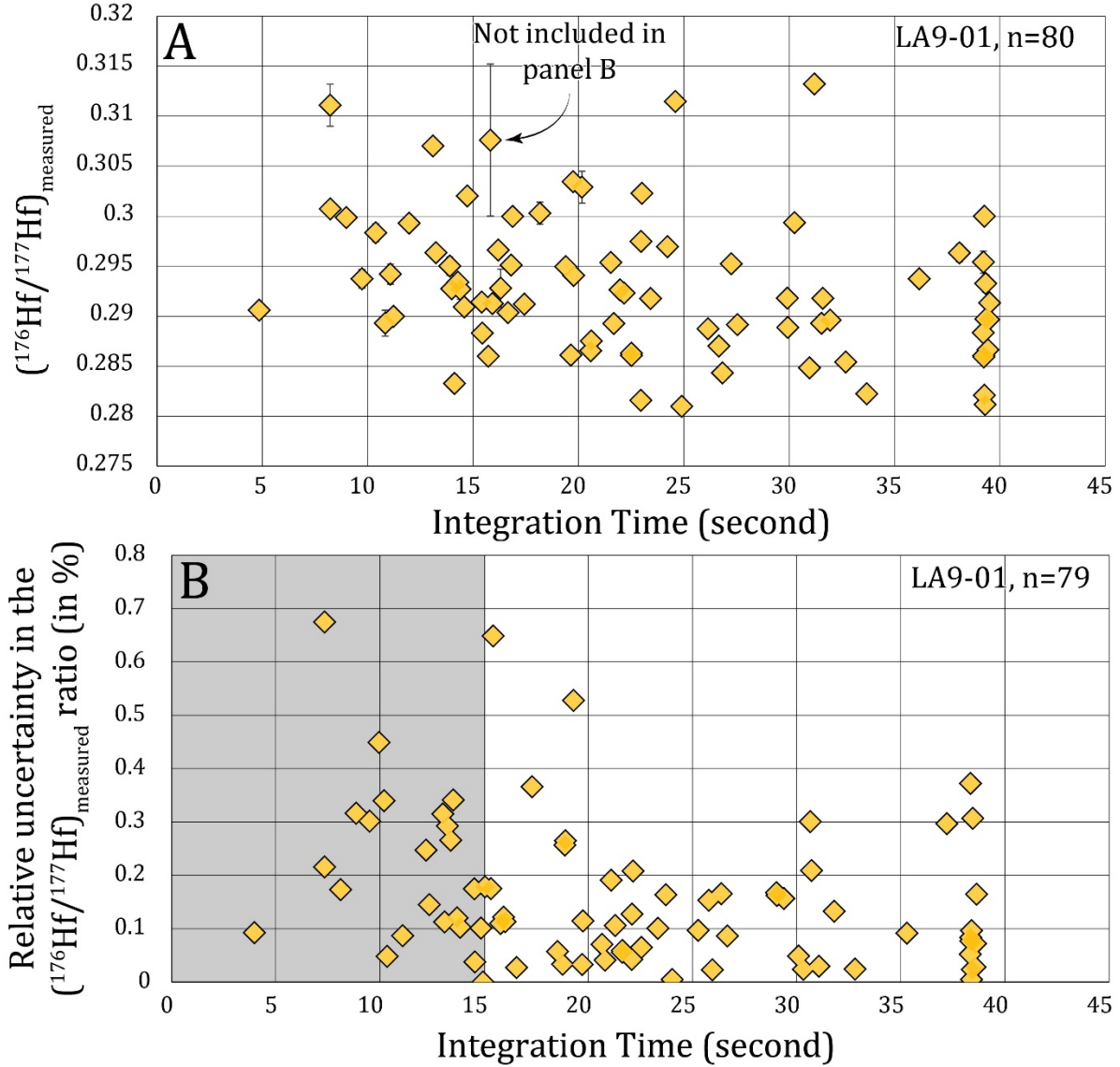


**Figure 7:** A.  $(^{176}\text{Hf}/^{177}\text{Hf})_{\text{measured}}$  ratio versus Integration time (in second) for each individual analysis of unknown. No correlation between these two variables is observed, indicating inter-independence. Uncertainty bars are absolute internal two Standard Error (2 S.E.). B. Relative 2 S.E. internal uncertainty of the  $(^{176}\text{Hf}/^{177}\text{Hf})_{\text{measured}}$  ratio expressed in per cent versus the Integration time (in second). Green diamond represents individual U–Th–Pb/Lu–Yb–Hf LASS unknown analysis carried out in this contribution. The grey area represents Integration time < 15 seconds. Due to the higher variability in the relative error value of LASS analyses within the grey area, these analyses were filtered out from the subsequent calculations.

Strikingly, the range of  $^{176}\text{Yb}/^{177}\text{Hf}$  ratio displayed by zircon reference material ( $[1.079 \cdot 10^{-3}; 1.432 \cdot 10^{-1}]$ ) covers 97.8% of the range of  $^{176}\text{Yb}/^{177}\text{Hf}$  ratio displayed by the unknown zircon grains investigated in this contribution ( $[4.25 \cdot 10^{-4}; 3.140 \cdot 10^{-2}]$ ), only 2 analyses, out of 80, show a  $^{176}\text{Yb}/^{177}\text{Hf}$  ratio below the minimal value of Mud Tank zircon reference material. This in addition to the fact that the  $^{176}\text{Yb}/^{173}\text{Yb}$  isotope ratio is adjusted in the DRS to reflect the daily drift of the MC-SF-ICP-MS (i.e. adjusted for each

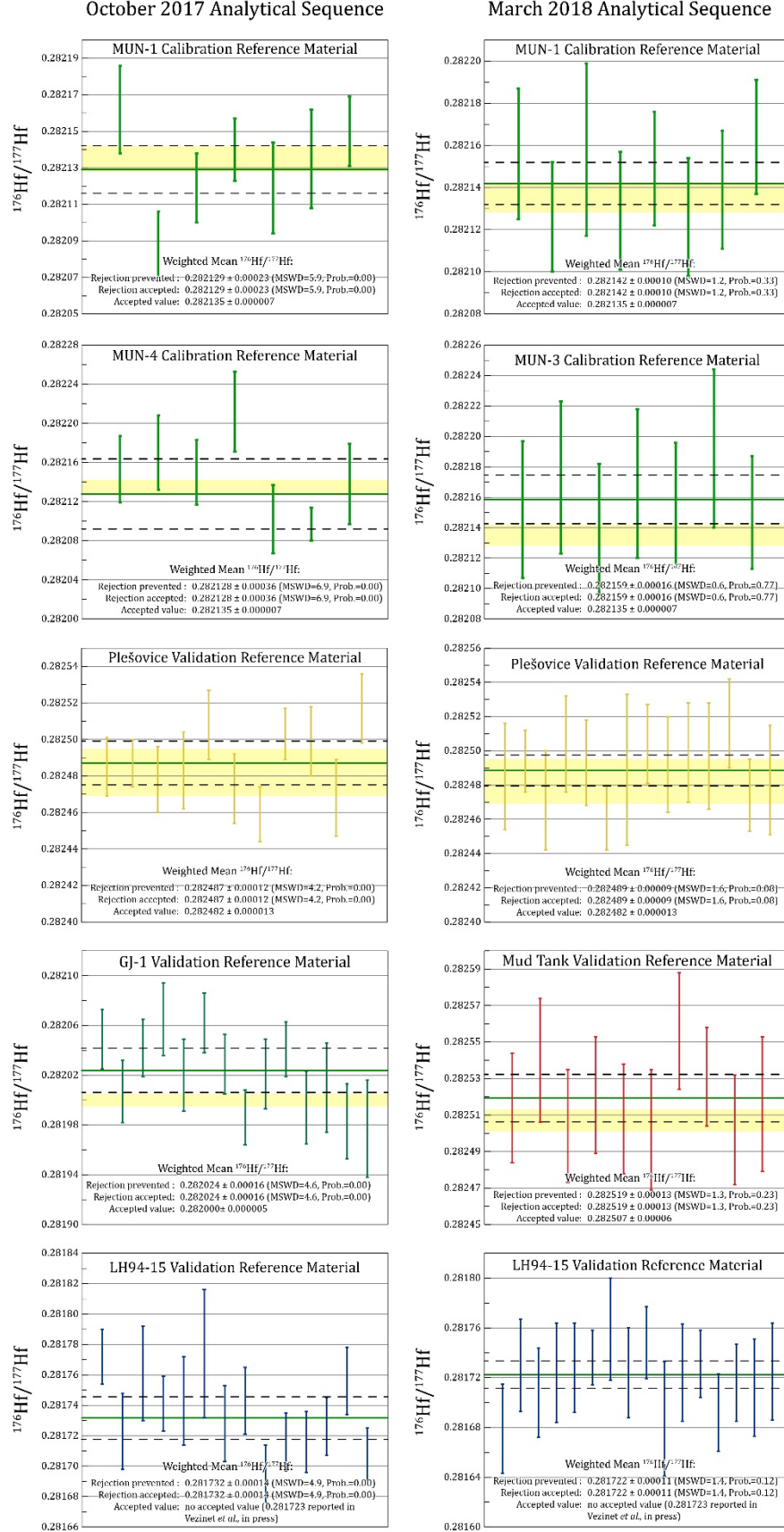
single sequence of analyses) provide a high degree of confidence in Yb-correction for the analyses produced in this contribution.

Moreover, it is worth noting that the selected integration time does not affect the absolute  $^{176}\text{Hf}/^{177}\text{Hf}$  ratio (Figure 7A). This implies that when considering the  $^{176}\text{Hf}/^{177}\text{Hf}$  ratio, all analysis have the same statistical weight. Nonetheless, integration time affects the uncertainty relative to each individual analysis (Figure 7B). Decreasing integration time increases the relative uncertainty of the  $(^{176}\text{Hf}/^{177}\text{Hf})_{\text{corrected}}$  ratios. Consequently, individual LASS analyses with integration time lower than 15 seconds were screened out from subsequent calculations.

#### 2.4.4 $^{176}\text{Hf}/^{177}\text{Hf}$ weighted mean

Figure 8 presents the distribution of  $^{176}\text{Hf}/^{177}\text{Hf}$  ratios for each sequence of analyses conducted during this study and for each zircon reference material. The weighted mean of measurements performed on MUN-1, MUN-4 synthetic zircon on one hand and on the natural zircon (Mud Tank, Plešovice, GJ-1) on the other hand are in perfect agreement with the ratio determined by solution MC-ICP-MS analyses (yellow band in Figure 8), see Fisher *et al.* (2011); Woodhead and Hergt (2005); Sláma *et al.* (2008) and Morel *et al.* (2008), respectively, for reference values.

**Figure 8:**  $^{176}\text{Hf}/^{177}\text{Hf}$  weighted averages relative to zircon reference material used in this contribution. Colour code is a function of the zircon reference material. Vertical bars are individual analyses with absolute internal 2 S.E. length. The green horizontal bar represents the value of the weighted mean (in the *rejection prevented* case), dotted horizontal lines represent the absolute 2 S.E. of the weighted mean. The yellow area represents the value and absolute 2 S.E. uncertainty of the reference value. There is no published  $^{176}\text{Hf}/^{177}\text{Hf}$  ratio for the LH94-15 zircon reference material, the weighted average diagram is reported to show the good consistency through the course of a single sequence of analyses and between sequences. Value of MUN-1/MUN-4; GJ-1; Plešovice and Mud Tank zircon reference material are from Fisher *et al.* (2011), Morel *et al.* (2008), Sláma *et al.* (2008) and Woodhead and Hergt (2005) respectively.



## 2.5 U–Pb Tera-Wasserburg diagram

Figure 9 shows the U–Pb ellipses of the analyses carried out throughout this study and the discordia line built with the analyses that passed the filtering detailed in the Methods section of the main manuscript.

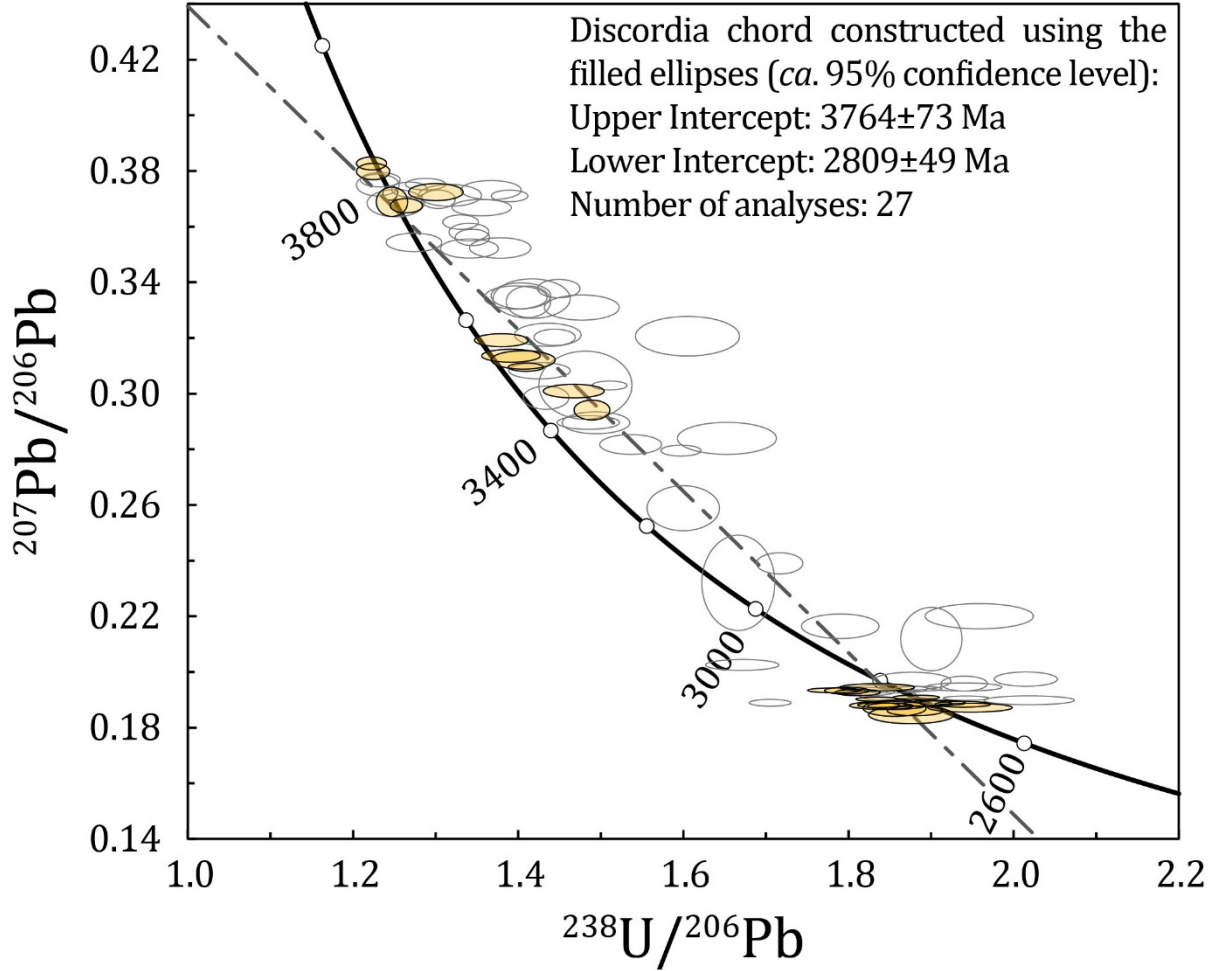


**Figure 9: Tera-Wasserburg diagram of the zircon analyses produced in this study. The discordia line has been constructed with the analyses that passed the filtering detailed in the Methods section of the main manuscript (n=27). Ellipses are reported at a coverage factor of 2 (ca. 95% confidence level).**



### 3 Ion probe zircon oxygen-isotope measurements<sup>2</sup>

Mount preparation was carried out at the Canadian Centre for Isotopic Microanalysis (CCIM), University of Alberta. Polished mid-sections of zircon were exposed within two 25 mm diameter epoxy mounts (M1483) using diamond grits. The mount was cleaned with a lab soap solution and de-ionized  $\text{H}_2\text{O}$ . The mount was coated with 10 nm of high-purity Au prior to scanning electron microscopy (SEM) utilizing a Zeiss EVO MA15 instrument equipped with a high-sensitivity, broadband cathodoluminescence (CL) and backscattered electron detectors. Beam conditions were 15kV and 3 – 5 nA sample current. A further 40 nm of Au was subsequently deposited on the mount prior to SIMS analysis.

Oxygen isotopes ( $^{18}\text{O}$ ,  $^{16}\text{O}$ ) in zircon were analysed using a Cameca IMS 1280 multicollector ion microprobe (CCIM, University of Alberta). A  $^{133}\text{Cs}^+$  primary beam was operated with impact energy of 20 keV and beam current of 1.5 – 2.0 nA. The  $\sim 10\ \mu\text{m}$  diameter probe was rastered ( $20 \times 20\ \mu\text{m}$ ) for 45 s prior to acquisition, and then  $6 \times 6\ \mu\text{m}$  during acquisition, forming analysed areas  $\sim 15\ \mu\text{m}$  across and  $\sim 2\ \mu\text{m}$  deep. The normal incidence electron gun was utilized for charge compensation. Negative secondary ions were extracted through 10 kV into the secondary (Transfer) column. Transfer conditions included a 122  $\mu\text{m}$  entrance slit, a  $5 \times 5\ \text{mm}$  pre-ESA (field) aperture, and 100x sample magnification at the field aperture, transmitting all regions of the sputtered area. No energy filtering was employed. The mass/charge separated oxygen ions were detected simultaneously in Faraday cups L'2 ( $^{16}\text{O}^-$ ) and H'2 ( $^{18}\text{O}^-$ ) at mass resolutions ( $m/\Delta m$  at 10%) of 1950 and 2250, respectively. Secondary ion count rates for  $^{16}\text{O}^-$  and  $^{18}\text{O}^-$  were typically  $\sim 2 \times 10^9$  and  $4 \times 10^6$  counts/s utilizing  $10^{10}\ \Omega$  and  $10^{11}\ \Omega$  amplifier circuits, respectively. Faraday cup baselines were measured at the start of the analytical session. A single analysis took 280 s, including pre-analysis rastering, automated secondary ion tuning, and 75 s of continuous peak counting.

Instrumental mass fractionation (IMF) was monitored by repeated analysis of the zircon primary reference material (S0081= UAMT1 with  $\delta^{18}\text{O}_{\text{VSMOW}} = +4.87$ ; R. Stern, unpublished laser fluorination data, University of Oregon), once after every four unknowns, in addition to TEM2 ( $\delta^{18}\text{O}_{\text{VSMOW}} = +8.2\ \text{‰}$ ; Black *et al.*, 2004) after every 8 unknowns. The  $^{18}\text{O}^-/^{16}\text{O}^-$  data set for the primary RM S0081 was processed collectively for three analytical sessions ( $N = 43, 23, 46$ ), yielding standard deviations of 0.09 ‰, 0.09 ‰, and 0.08 ‰, following correction for systematic within-session drift of  $\leq 0.3\ \text{‰}$ . Overall IMF was  $< 0.6\ \text{‰}$ . The individual spot uncertainties for the unknowns at 95% confidence for  $\delta^{18}\text{O}_{\text{VSMOW}}$  include errors relating to within-spot counting statistics, between-spot (geometric) effects, and correction for instrumental mass fractionation, and average  $\pm 0.20 - 0.25\ \text{‰}$ . Results for multiple spots on multiple

---

<sup>2</sup> Section 3 and Section 4 are identical to those reported in the Electronic Supplementary Material of Vezinet *et al.* (2018).

grains of the secondary RM (TEM2) gave mean session values for  $\delta^{18}\text{O}_{\text{VSMOW}} = +8.28 \pm 0.04 \text{ ‰}$  (MSWD = 0.88; N = 28; SD = 0.10 ‰), see Table 2.

**Table 2: Analytical performance of the ion probe zircon oxygen-isotope measurement performed in the course of this study. RM: Reference Material. SE: Standard Error.**

Analytical Performance	02/06-07/2018 – IP18009	
	Calibration RM	Validation RM
Systematic drift in IMF	0.1 ‰	Ø
Standard deviation of drift corrected	0.08 ‰	0.1 ‰
Instrumental mass fractionation $\alpha$	1.000098104	Ø
$\Delta$ measured - accepted	0.1 ‰	Ø
spot-to-spot excess error added (68% conf)	0.005 ‰	Ø
calibration mean error added (68% conf)	0.0014 ‰	Ø
median uncertainty (95% conf) excluding uncertainty in reference value	0.22 ‰	0.21 ‰
number of RM spots	46	28
$\delta^{18}\text{O}$ value (‰) $\pm$ 2SE	Ø	8.28 $\pm$ 0.04 MSWD = 0.88
Number of spots analysed on unknowns	152	
Median uncertainty (95% conf) without RM value uncertainty	0.21 ‰	

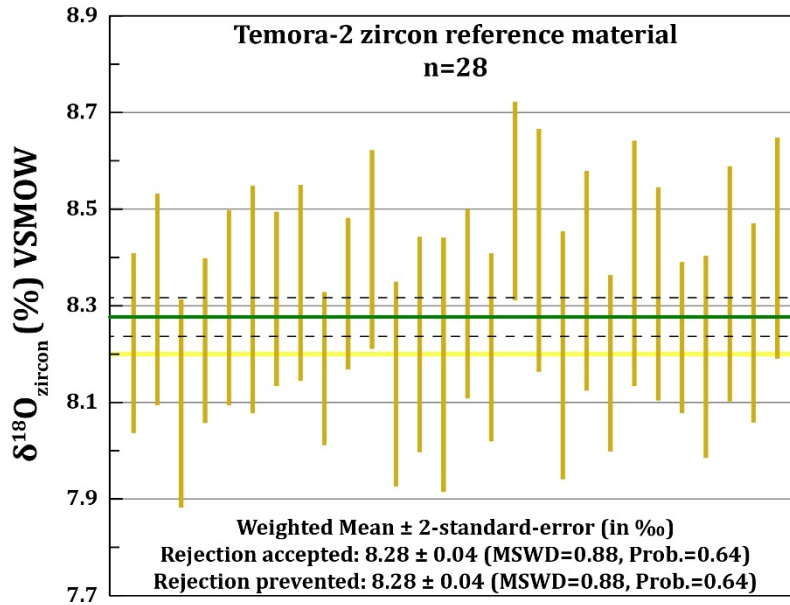


**Figure 10: Weighted mean  $\pm$  2-standard-error (in ‰) of the Temora-2 zircon validation material used for ion-probe oxygen isotope analyses. The horizontal green bar represents the mean of the run, dotted lines are the uncertainty associated to the mean value. The horizontal yellow line represent the accepted value of Black *et al.* (2004). Verticals bars, and uncertainty in the mean are reported at a coverage factor of 2. Notably, this ion-probe O isotope analytical session is the same from which the zircon O isotope data presented in Vezinet *et al.* (2018) have been produced.**

## 4 Zircon trace element analyses

### 4.1 Method for trace element analyses by LA-ICP-MS

Trace element data were obtained on mounted zircon separates using (spatially resolved) laser ablation coupled with sector field inductively coupled plasma-mass spectrometry (LA-SF-ICP-MS) at the University of Alberta. The mass spectrometer was operated in low mass resolution ( $M/\Delta M \approx 300$ ) with guard electrode off mode. The laser ablation used was a Resolution 193nm excimer laser system equipped with a two-volume S155 sample cell (Laurin Technic). The cell was pressurized with high-purity He gas and mixed in the cell with Ar and nitrogen. Zircon grains were ablated using 33  $\mu\text{m}$  craters and an 8 Hz repetition with the laser energy at the target (fluence) regulated at  $\sim 4 \text{ J/cm}^2$ . An analysis comprised 40 s of background gas collection followed by 50 s of ablation. The ICP-MS was operated at 1300W and a torch depth of 3.5 mm. Argon (0.8–1L/min), Helium ( $\sim 350 \text{ ml/min}$ ) and nitrogen gas flow ( $\sim 1 \text{ ml/min}$ ), torch position and focusing potentials were optimized in order to achieve optimal signals on Co, La and Th and low oxide production rates ( $\text{ThO/Th} < 0.2\%$ ) as well as plasma robustness ( $^{238}\text{U}^+/^{232}\text{Th}^+ \approx 1$ ). Calibration was performed using NIST SRM 612 in conjunction with internal standardization using isotope  $^{29}\text{Si}$ . All data were reduced offline using Iolite v3.32 (Paton *et al.*; <https://iolite-software.com/>). The results of the secondary standards (e.g., zircon 91500) agree with the reference values within relative uncertainties of typical 5–10% or better at the 95%-confidence level. The detection limits are below 0.1 ppm for most elements and in run precisions were within 10%.

Data reduction of the trace element analyses was carried out using the same software we used for the LASS analyses (Igor Pro + Iolite). Therefore, any non-zircon inclusions encountered through the course of each analysis can be identified through careful examination of the time-resolved data displayed in Igor Pro/Iolite software (e.g. P for monazite/xenotime, Al/Fe for allanite, etc...). Although contamination from non-zircon inclusions can occur during spatially resolved mineral analysis, our data reduction workflow enables us to easily identify and screen out such analyses.

### 4.2 Chemical screening

To better identify secondary alteration processes in the zircon sample population, we used the trace element content measured during this study. The trace element systematics of zircon domains have been shown to be useful in identifying altered zircon domains (e.g. Krogh and Davis, 1975; Geisler and Schleicher, 2000; Geisler *et al.*, 2001; Geisler *et al.*, 2003; Rayner *et al.*, 2005). We used a threshold of 300 ppm for the Ca content, above which the zircon domain is deemed to be altered (value ranging between those of the altered zircon domains and unaltered zircon domains determined by Rayner *et al.*, 2005). Next, we screened out all analyses with Ba contents above 0.4 ppm, which were shown to

correspond to altered zircon domains by Rayner *et al.* (2005). Then, we selected analyses with negligible common Pb, i.e. with  $f^{206}\text{Pb}_c$  values  $< 0.1\%$ , which is an order of magnitude lower than the typical uncertainty in the  $^{207}\text{Pb}/^{206}\text{Pb}$  date obtained in this study. Based on this chemical screening, together with the analytical filtering presented in the Method section of the main manuscript) we selected the least disturbed analyses of the whole dataset.

As demonstrated in Figure 12, domains featuring internal micro-structures typically interpreted as resulting from alteration processes, also show elevated Ca and Ba contents, benchmarking our selection procedure against the study of Rayner *et al.* (2005).

#### 4.1 Trace element composition of optically disturbed zircon domains

Figure 11 shows the trace element concentration of optically altered zircon domains and demonstrates that at least one of the chemical determinant (Ca,  $(\text{La})_N$  and  $(\text{La}/\text{Sm})_N$ ) is above the normal range displayed by igneous zircons. In this zircon sample population, the Ca content is the one that shows the most significant abnormal increase. This illustrates that secondary alteration processes can be identified by the trace element analyses carried out in this study.

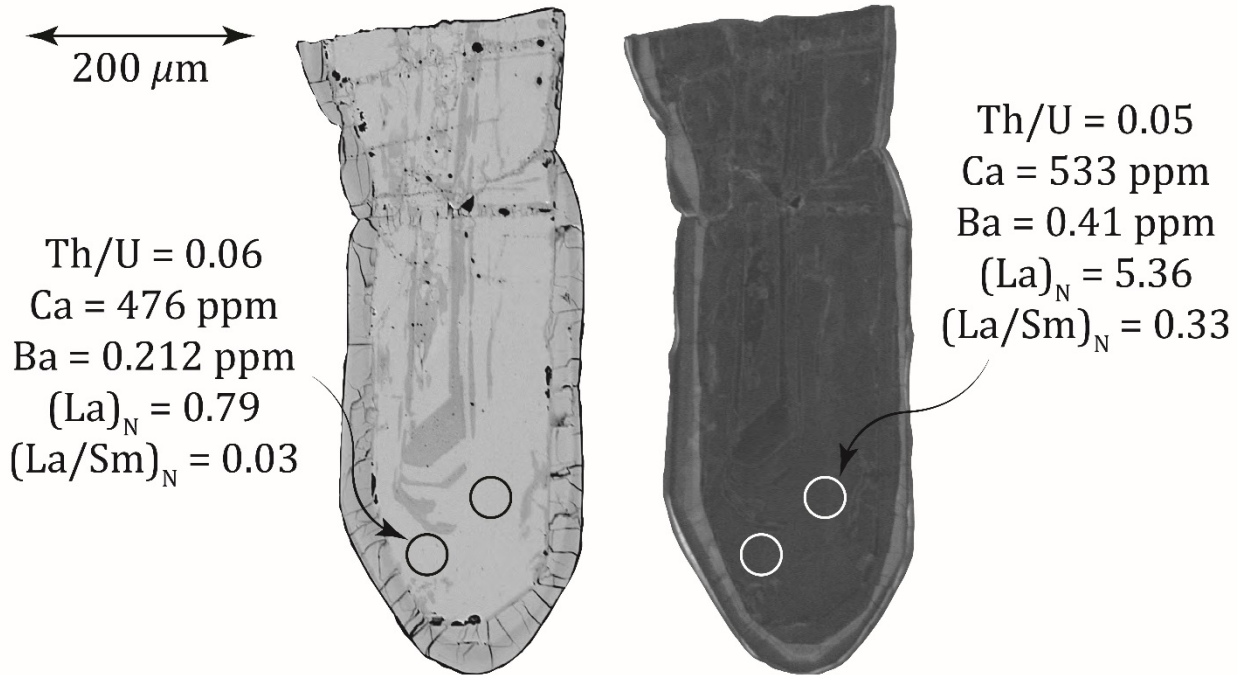


Figure 11: Trace element content of altered zircon domains. Note that the alteration is mainly visible in the back-scattered electron (BSE) image, not on the cathodoluminescence (CL) image. Spot size: 33  $\mu\text{m}$ .

## 5 The role of the $^{176}\text{Lu}/^{177}\text{Hf}$ ratio in the evolution of the Hf signature

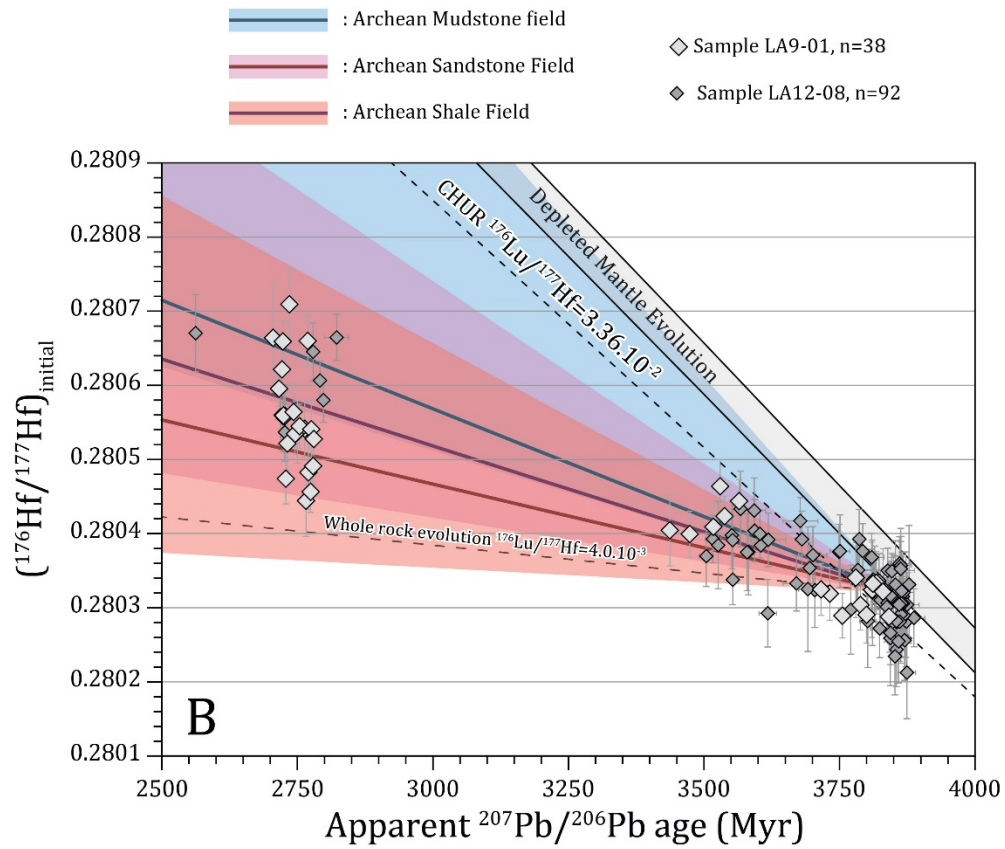
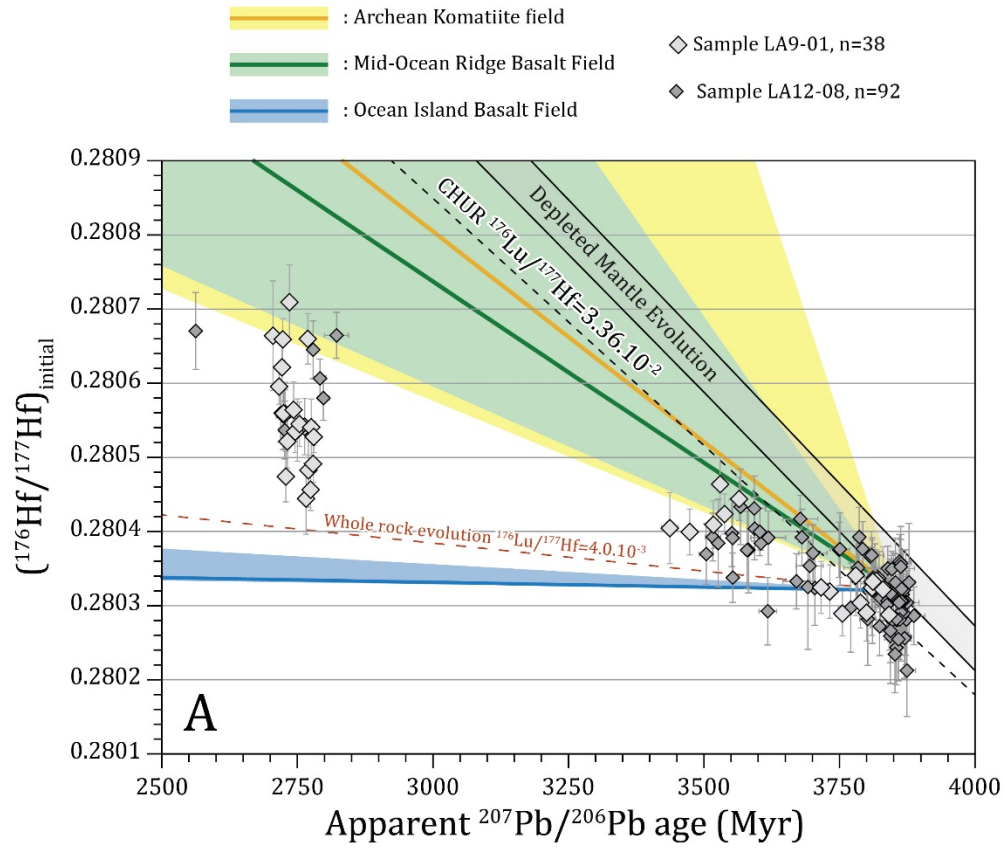
Figure 12 reports the  $(^{176}\text{Hf}/^{177}\text{Hf})_{\text{initial}}$  versus Apparent  $^{207}\text{Pb}/^{206}\text{Pb}$  age carried out by the LASS method during this study and that of Vezinet *et al.* (2018). In addition, Figure 12 shows the field of  $^{176}\text{Hf}/^{177}\text{Hf}$  compositions as a function of varied  $^{176}\text{Lu}/^{177}\text{Hf}$  ratios through time (chemically basic rocks in Figure 12A and sediments in Figure 12B). It clearly appears that, while all fields broadly overlap, median  $^{176}\text{Lu}/^{177}\text{Hf}$  ratios of chemically basic rock are higher than those of the sediments.

Therefore, if considering the Hf isotope composition observed during the Paleoproterozoic reworking event at *ca.* 3.5Gyr, as well as the range observed during the Neoproterozoic event at 2.7-2.8 Gyr result from mixing with an external component, then mixing with chemically basic rocks appears to be a likely option.

Evolution lines have been constructed using the following references: Patchett and Tatsumoto (1980); Salters (1996); Blichert-Toft and Arndt (1999); Vervoort *et al.* (1999); Blichert-Toft and Puchtel (2010); Nebel *et al.* (2014); Blichert-Toft *et al.* (2015); Garçon *et al.* (2017); and Hoffmann and Wilson (2017).

**Figure 12: Effect on the  $^{176}\text{Lu}/^{177}\text{Hf}$  ratio on the evolution of the  $^{176}\text{Hf}/^{177}\text{Hf}$  ratio after time integration. Fields are built using the range of  $^{176}\text{Lu}/^{177}\text{Hf}$  ratios for each relevant lithology; bold lines represent the median  $^{176}\text{Lu}/^{177}\text{Hf}$  ratio for each relevant range.**





## 6 Compiled dataset of zircon $\delta^{18}\text{O}$ value

The compiled dataset of igneous and metamorphic zircon from (meta)-igneous rocks (n=454) presented in Figure 2B of the main manuscript reports spatially resolved analyses of combined U–Pb/O isotopes. The zircon  $\delta^{18}\text{O}$  dataset compiled for this study reports only concordant 95-105% U–Pb analyses because previous studies suggested an effect of discordance on the  $\delta^{18}\text{O}$  value in zircon (Booth *et al.*, 2005). In addition, the compiled dataset presented in Figure 2B of the main manuscript only depicts zircon analyses from (meta)-igneous rocks: i.e. analyses of magmatic and metamorphic domains of zircon grains extracted from either pristine un-deformed igneous rocks or deformed/metamorphosed igneous rocks. Analyses of detrital zircon grains (and their metamorphic overgrowths) from (meta)-sedimentary lithologies are excluded from this plot.

Data from: the São Francisco craton (Albert *et al.*, 2016); the Southern Superior Province (Bowman *et al.*, 2011); the Ukrainian Shield (Claesson *et al.*, 2016); the Tarim Craton (Ge *et al.*, 2014); the Yangtze craton (Guo *et al.*, 2014); the Yilgarn craton (Hammerli *et al.*, 2018); the North Atlantic craton (Hiess *et al.*, 2009; Hiess *et al.*, 2011); the North Australian craton (Hollis *et al.*, 2014); the Pilbara craton (Kitajima *et al.*, 2012); the North China craton (Liu *et al.*, 2009; Wan *et al.*, 2013; Wang *et al.*, 2018); The Grunehogna craton (Marschall *et al.*, 2010); the Nagssugtoqidian Orogen (Nicolli *et al.*, 2017) and the Slave craton (Reimink *et al.*, 2014; Reimink *et al.*, 2016).

## 7 Uncertainty propagation workflow<sup>3</sup>

### 7.1 Uncertainty on the U–Th–Pb isotope ratios and dates

Uncertainties relative to the U–Th–Pb isotope system are values produced by the uncertainty propagation workflow built into Iolite software.

### 7.2 Uncertainty on the $(^{176}\text{Hf}/^{177}\text{Hf})_{\text{initial}}$ ratio

Uncertainty on the  $(^{176}\text{Hf}/^{177}\text{Hf})_{\text{App}}$  ratio is calculated using the rule for the propagation of uncertainty in multiple variable functions (see for example [Hughes and Hase, 2010](#)). For better clarity, the complex uncertainty propagation equation is decomposed into elementary functions that can be easily treated. In the following, the term  $s[x]$  stands for the absolute uncertainty of the term in brackets ( $x$  in this case).

1.  $s[\lambda(^{176}\text{Lu}) \times t] = (\lambda(^{176}\text{Lu}) \times t) \times \sqrt{\left(\frac{s[^{176}\text{Lu}]}{^{176}\text{Lu}}\right)^2 + \left(\frac{s[t]}{t}\right)^2} = s_1$
2.  $s[\exp(\lambda(^{176}\text{Lu}) \times t)] = \exp(\lambda(^{176}\text{Lu}) \times t) \times s_1 = s_2$
3.  $s[\exp(\lambda(^{176}\text{Lu}) \times t) - 1] = s_2$
4.  $s\left[\frac{^{176}\text{Lu}}{^{177}\text{Hf}} \times (\exp(\lambda(^{176}\text{Lu}) \times t) - 1)\right] =$   
 $\left(\frac{^{176}\text{Lu}}{^{177}\text{Hf}} \times (\exp(\lambda(^{176}\text{Lu}) \times t) - 1)\right) \times \sqrt{\left(\frac{s[^{176}\text{Lu}/^{177}\text{Hf}]}{^{176}\text{Lu}/^{177}\text{Hf}}\right)^2 + \left(\frac{s_2}{\exp(\lambda(^{176}\text{Lu}) \times t) - 1}\right)^2} = s_3$
5.  $s\left[\frac{^{176}\text{Hf}}{^{177}\text{Hf}} - \frac{^{176}\text{Lu}}{^{177}\text{Hf}} \times (\exp(\lambda(^{176}\text{Lu}) \times t) - 1)\right] = \sqrt{\left(\frac{s_3}{\frac{^{176}\text{Lu}}{^{177}\text{Hf}} \times (\exp(\lambda(^{176}\text{Lu}) \times t) - 1)}\right)^2 + \left(\frac{s[(^{176}\text{Hf}/^{177}\text{Hf})_{\text{corr}}]}{(^{176}\text{Hf}/^{177}\text{Hf})_{\text{corr}}}\right)^2}$   
 $= s\left[\left(\frac{^{176}\text{Hf}}{^{177}\text{Hf}}\right)_{\text{App/Ini}}\right]$

It is noteworthy that uncertainty in the  $(^{176}\text{Hf}/^{177}\text{Hf})_{\text{Apparent/Initial}}$  ratio is highly dominated by the internal uncertainty of the  $(^{176}\text{Hf}/^{177}\text{Hf})_{\text{Corrected}}$  ratio. Uncertainties on (i) the  $^{207}\text{Pb}/^{206}\text{Pb}$  dates, (ii) the decay-constant  $\lambda(^{176}\text{Lu})$  and (iii) the  $(^{176}\text{Lu}/^{177}\text{Hf})$  chemical ratio are minor with regards to the internal uncertainty of the  $(^{176}\text{Hf}/^{177}\text{Hf})_{\text{Corrected}}$  ratio. This calculation must be performed for both the

<sup>3</sup> Sections 6 and 7 are identical to those reported in [Vezinet \*et al.\* \(2018\)](#).

$(^{176}\text{Hf}/^{177}\text{Hf})_{\text{Apparent/Initial}}$  ratio of the unknown and the corresponding  $(^{176}\text{Hf}/^{177}\text{Hf})$  ratio of the geochemical reservoir used for the calculation of the  $\varepsilon$  value (commonly the Chondritic Uniform Reservoir, values after [Bouvier \*et al.\*, 2008](#)).

### 7.3 Uncertainty on the $\varepsilon(\text{Hf})$ ratio

The uncertainty on the  $\varepsilon(\text{Hf})$  value is calculated in a similar way to the uncertainty on the  $(^{176}\text{Hf}/^{177}\text{Hf})_{\text{Apparent/Initial}}$ , i.e. through rules of uncertainty propagation for multiple variable functions. It results in:

$$s[\varepsilon(\text{Hf})] = \sqrt{\left(\frac{s[(^{176}\text{Hf}/^{177}\text{Hf})_{\text{App/Ini}}]}{(^{176}\text{Hf}/^{177}\text{Hf})_{\text{App/Ini}}}\right)^2 + \left(\frac{s[(^{176}\text{Hf}/^{177}\text{Hf})_{\text{CHUR}}]}{(^{176}\text{Hf}/^{177}\text{Hf})_{\text{CHUR}}}\right)^2} \times 10^4$$

## 8 Methodology for the determination of whole-rock major- and trace-elements composition

Whole-rock chemical composition of the investigated rock were determined at the Service d'Analyse de Roches et Minéraux (SARM). A thorough description of the methodology is reported in [Carignan \*et al.\* \(2001\)](#). The only difference with [Carignan \*et al.\* \(2001\)](#) is the mass-spectrometer devices used at the present day. The SARM is currently using iCap6500 and iCapQ (both ThermoFisher instruments) as ICP-AES and ICP-MS devices respectively.

## References

- Albert, C., Farina, F., Lana, C., Stevens, G., Storey, C., Gerdes, A. and Dopico, C. M., 2016, Archean crustal evolution in the Southern São Francisco craton, Brazil: Constraints from U-Pb, Lu-Hf and O isotope analyses: *Lithos*, v. 266, p. 64-86, doi: 10.1016/j.lithos.2016.09.029.
- Ashton, K., Heaman, L., Lewry, J., Hartlaub, R. and Shi, R., 1999, Age and origin of the Jan Lake Complex: a glimpse at the buried Archean craton of the Trans-Hudson Orogen: *Canadian Journal of Earth Sciences*, v. 36, no. 2, p. 185-208, doi: 10.1139/e98-038.
- Baadsgaard, H., Collerson, K. D. and Bridgwater, D., 1979, The Archean gneiss complex of northern Labrador. 1. Preliminary U-Th-Pb geochronology: *Canadian Journal of Earth Sciences*, v. 16, no. 4, p. 951-961, doi: 10.1139/e79-081.
- Black, L. P., Kamo, S. L., Allen, C. M., Davis, D. W., Aleinikoff, J. N., Valley, J. W., Mundil, R., Campbell, I. H., Korsch, R. J. and Williams, I. S., 2004, Improved  $^{206}\text{Pb}/^{238}\text{U}$  microprobe geochronology by the monitoring of a trace-element-related matrix effect; SHRIMP, ID-TIMS, ELA-ICP-MS and oxygen isotope documentation for a series of zircon standards: *Chemical Geology*, v. 205, no. 1, p. 115-140, doi: 10.1016/j.chemgeo.2004.01.003.
- Blichert-Toft, J. and Arndt, N. T., 1999, Hf isotope compositions of komatiites: *Earth and Planetary Science Letters*, v. 171, no. 3, p. 439-451, doi: 10.1016/S0012-821X(99)00151-X.
- Blichert-Toft, J. and Puchtel, I. S., 2010, Depleted mantle sources through time: evidence from Lu-Hf and Sm-Nd isotope systematics of Archean komatiites: *Earth and Planetary Science Letters*, v. 297, no. 3, p. 598-606, doi: 10.1016/j.epsl.2010.07.012.
- Blichert-Toft, J., Arndt, N. T., Wilson, A. and Coetzee, G., 2015, Hf and Nd isotope systematics of early Archean komatiites from surface sampling and ICDP drilling in the Barberton Greenstone Belt, South Africa: *American Mineralogist*, v. 100, no. 11-12, p. 2396-2411, doi: 10.2138/am-2015-5325.
- Booth, A. L., Kolodny, Y., Chamberlain, C. P., McWilliams, M., Schmitt, A. K. and Wooden, J., 2005, Oxygen isotopic composition and U-Pb discordance in zircon: *Geochimica et Cosmochimica Acta*, v. 69, no. 20, p. 4895-4905, doi: 10.1016/j.gca.2005.05.013.
- Bouvier, A., Vervoort, J. D. and Patchett, P. J., 2008, The Lu-Hf and Sm-Nd isotopic composition of CHUR: constraints from unequilibrated chondrites and implications for the bulk composition of terrestrial planets: *Earth and Planetary Science Letters*, v. 273, no. 1, p. 48-57, doi: 10.1016/j.epsl.2008.06.010.
- Bowman, J. R., Moser, D. E., Valley, J. W., Wooden, J. L., Kita, N. T. and Mazdab, F. K., 2011, Zircon U-Pb isotope,  $\delta^{18}\text{O}$  and trace element response to 80 my of high temperature metamorphism in the lower crust: Sluggish diffusion and new records of Archean craton formation: *American Journal of Science*, v. 311, no. 9, p. 719-772, doi: 10.2475/09.2011.01.
- Brown, M., 1973, The Definition of Metatexis, Diatexis and Migmatite: *Proceedings of the Geologists' Association*, v. 84, no. 4, p. 371-382, doi: 10.1016/S0016-7878(73)80021-5.
- Carignan, J., Hild, P., Mevelle, G., Morel, J. and Yeghicheyan, D., 2001, Routine analyses of trace elements in geological samples using flow injection and low pressure on-line liquid chromatography coupled to ICP-MS: a study of geochemical reference materials BR, DR-N, UB-N, AN-G and GH: *Geostandards and Geoanalytical Research*, v. 25, no. 2-3, p. 187-198, doi: 10.1111/j.1751-908X.2001.tb00595.x.



- Claesson, S., Bibikova, E. V., Shumlyanskyy, L., Whitehouse, M. J. and Billström, K., 2016, Can oxygen isotopes in magmatic zircon be modified by metamorphism? A case study from the Eoarchean Dniester-Bug Series, Ukrainian Shield: *Precambrian Research*, v. 273, p. 1-11, doi: 10.1016/j.precamres.2015.11.002.
- Fisher, C. M., Hanchar, J. M., Samson, S. D., Dhuime, B., Blichert-Toft, J., Vervoort, J. D. and Lam, R., 2011, Synthetic zircon doped with hafnium and rare earth elements: a reference material for in situ hafnium isotope analysis: *Chemical Geology*, v. 286, no. 1, p. 32-47, doi: 10.1016/j.chemgeo.2011.04.013.
- Fisher, C. M., Vervoort, J. D. and Hanchar, J. M., 2014, Guidelines for reporting zircon Hf isotopic data by LA-MC-ICPMS and potential pitfalls in the interpretation of these data: *Chemical geology*, v. 363, p. 125-133, doi: 10.1016/j.chemgeo.2013.10.019.
- Fisher, C. M., Paton, C., Pearson, D. G., Sarkar, C., Luo, Y., Tersmette, D. B. and Chacko, T., 2017, Data Reduction of Laser Ablation Split-Stream (LASS) Analyses Using Newly Developed Features Within Iolite: With Applications to Lu-Hf+U-Pb in Detrital Zircon and Sm-Nd+U-Pb in Igneous Monazite: *Geochemistry, Geophysics, Geosystems*, v. 18, no. 12, p. 4604-4622, doi: 10.1002/2017GC007187.
- Garçon, M., Carlson, R., Shirey, S., Arndt, N., Horan, M. and Mock, T., 2017, Erosion of Archean continents: The Sm-Nd and Lu-Hf isotopic record of Barberton sedimentary rocks: *Geochimica et Cosmochimica Acta*, v. 206, p. 216-235, doi: 10.1016/j.gca.2017.03.006.
- Ge, R., Zhu, W., Wilde, S. A., Wu, H., He, J. and Zheng, B., 2014, Archean magmatism and crustal evolution in the northern Tarim Craton: insights from zircon U-Pb-Hf-O isotopes and geochemistry of ~2.7 Ga orthogneiss and amphibolite in the Korla Complex: *Precambrian Research*, v. 252, p. 145-165, doi: 10.1016/j.precamres.2014.07.019.
- Geisler, T. and Schleicher, H., 2000, Improved U-Th-total Pb dating of zircons by electron microprobe using a simple new background modeling procedure and Ca as a chemical criterion of fluid-induced U-Th-Pb discordance in zircon: *Chemical Geology*, v. 163, no. 1-4, p. 269-285, doi: 10.1016/S0009-2541(99)00099-6.
- Geisler, T., Ulonska, M., Schleicher, H., Pidgeon, R. T. and van Bronswijk, W., 2001, Leaching and differential recrystallization of metamict zircon under experimental hydrothermal conditions: *Contributions to Mineralogy and Petrology*, v. 141, no. 1, p. 53-65, doi: 10.1007/s004100000202.
- Geisler, T., Rashwan, A., Rahn, M., Poller, U., Zwingmann, H., Pidgeon, R., Schleicher, H. and Tomaschek, F., 2003, Low-temperature hydrothermal alteration of natural metamict zircons from the Eastern Desert, Egypt: *Mineralogical Magazine*, v. 67, no. 3, p. 485-508, doi: 10.1180/0026461036730112.
- Guo, J.-L., Gao, S., Wu, Y.-B., Li, M., Chen, K., Hu, Z.-C., Liang, Z.-W., Liu, Y.-S., Zhou, L. and Zong, K.-Q., 2014, 3.45 Ga granitic gneisses from the Yangtze Craton, South China: implications for Early Archean crustal growth: *Precambrian Research*, v. 242, p. 82-95, doi: 10.1016/j.precamres.2013.12.018.
- Hammerli, J., Kemp, A. I. and Jeon, H., 2018, An Archean Yellowstone? Evidence from extremely low  $\delta^{18}\text{O}$  in zircons preserved in granulites of the Yilgarn Craton, Western Australia: *Geology*, v. 46, no. 5, p. 411-414, doi: 10.1130/G39969.1.
- Hiess, J., Bennett, V. C., Nutman, A. P. and Williams, I. S., 2009, In situ U-Pb, O and Hf isotopic compositions of zircon and olivine from Eoarchaeal rocks, West Greenland: New insights to making old crust: *Geochimica et Cosmochimica Acta*, v. 73, no. 15, p. 4489-4516, doi: 10.1016/j.gca.2009.04.019.
- Hiess, J., Bennett, V. C., Nutman, A. P. and Williams, I. S., 2011, Archean fluid-assisted crustal cannibalism recorded by low  $\delta^{18}\text{O}$  and negative  $\varepsilon_{\text{Hf}(T)}$  isotopic signatures of West Greenland granite zircon: *Contributions to Mineralogy and Petrology*, v. 161, no. 6, p. 1027-1050, doi: 10.1007/s00410-010-0578-z.

- Hoffmann, J. E. and Wilson, A. H., 2017, The origin of highly radiogenic Hf isotope compositions in 3.33 Ga Comondale komatiite lavas (South Africa): *Chemical Geology*, v. 455, p. 6-21, doi: 10.1016/j.chemgeo.2016.10.010.
- Hollis, J., Van Kranendonk, M., Cross, A., Kirkland, C., Armstrong, R. and Allen, C. M., 2014, Low  $\delta^{18}\text{O}$  zircon grains in the Neoarchean Rum Jungle Complex, northern Australia: An indicator of emergent continental crust: *Lithosphere*, v. 6, no. 1, p. 17-25, doi: 10.1130/L296.1.
- Horstwood, M. S., Košler, J., Gehrels, G. E., Jackson, S. E., McLean, N. M., Paton, C., Pearson, N. J., Sircombe, K., Sylvester, P. and Vermeesch, P., 2016, Community-Derived Standards for LA- ICP- MS U- (Th- )Pb Geochronology–Uncertainty Propagation, Age Interpretation and Data Reporting: *Geostandards and Geoanalytical Research*, v. 40, no. 3, p. 311-332, doi: 10.1111/j.1751-908X.2016.00379.x.
- Hughes, I. and Hase, T., 2010, *Measurements and their uncertainties: a practical guide to modern error analysis*, New York, Oxford University Press, 153 p, ISBN: 0199566321.
- Jackson, S. E., Pearson, N. J., Griffin, W. L. and Belousova, E. A., 2004, The application of laser ablation-inductively coupled plasma-mass spectrometry to in situ U–Pb zircon geochronology: *Chemical Geology*, v. 211, no. 1, p. 47-69, doi: 10.1016/j.chemgeo.2004.06.017.
- Kitajima, K., Ushikubo, T., Kita, N. T., Maruyama, S. and Valley, J. W., 2012, Relative retention of trace element and oxygen isotope ratios in zircon from Archean rhyolite, Panorama Formation, North Pole Dome, Pilbara Craton, Western Australia: *Chemical Geology*, v. 332-333, p. 102-115, doi: 10.1016/j.chemgeo.2012.09.019.
- Krogh, T. and Davis, G., 1975, Alteration in zircons and differential dissolution of altered and metamict zircon: *Carnegie Institute Yearbook*, v. 74, p. 619-623
- Kusiak, M. A., Dunkley, D. J., Whitehouse, M. J., Wilde, S. A., Sałacińska, A., Konečný, P., Szopa, K., Gawęda, A. and Chew, D., 2018, Peak to post-peak thermal history of the Saglek Block of Labrador: a multiphase and multi-instrumental approach to geochronology: *Chemical Geology*, v. 484, p. 210-223, doi: 10.1016/j.chemgeo.2017.10.033.
- Liu, D., Wilde, S. A., Wan, Y., Wang, S., Valley, J. W., Kita, N., Dong, C., Xie, H., Yang, C., Zhang, Y. and Gao, L., 2009, Combined U–Pb, hafnium and oxygen isotope analysis of zircons from meta-igneous rocks in the southern North China Craton reveal multiple events in the Late Mesoarchean–Early Neoarchean: *Chemical Geology*, v. 261, no. 1, p. 140-154, doi: 10.1016/j.chemgeo.2008.10.041.
- Ludwig, K., 2012, *User's manual for Isoplot version 3.75–4.15: a geochronological toolkit for Microsoft: Excel* Berkley Geochronological Center Special Publication, no. 5
- Ludwig, K. R., 2003, *Isoplot/Ex version 3.00: a Geochronological Toolkit for Microsoft Excel*, Berkeley Geochronology Center, Berkeley, CA.
- Marschall, H. R., Hawkesworth, C. J., Storey, C. D., Dhuime, B., Leat, P. T., Meyer, H.-P. and Tamm-Buckle, S., 2010, The Annandagstoppane Granite, East Antarctica: evidence for Archaean intracrustal recycling in the Kaapvaal–Grunehogna Craton from zircon O and Hf isotopes: *Journal of Petrology*, v. 51, no. 11, p. 2277-2301, doi: 10.1093/petrology/egq057.
- Morel, M., Nebel, O., Nebel-Jacobsen, Y., Miller, J. and Vroon, P., 2008, Hafnium isotope characterization of the GJ-1 zircon reference material by solution and laser-ablation MC-ICPMS: *Chemical Geology*, v. 255, no. 1, p. 231-235, doi: 10.1016/j.chemgeo.2008.06.040.
- Moyen, J.-F., 2011, The composite Archaean grey gneisses: Petrological significance, and evidence for a non-unique tectonic setting for Archaean crustal growth: *Lithos*, v. 123, p. 21-36, doi: 10.1016/j.lithos.2010.09.015.

- Nebel, O., Campbell, I. H., Sossi, P. A. and Van Kranendonk, M. J., 2014, Hafnium and iron isotopes in early Archean komatiites record a plume-driven convection cycle in the Hadean Earth: *Earth and Planetary Science Letters*, v. 397, p. 111-120, doi: 10.1016/j.epsl.2014.04.028.
- Nicoli, G., Thomassot, E., Schannor, M., Vezinet, A. and Jovovic, I., 2017, Constraining a Precambrian Wilson Cycle lifespan: An example from the ca. 1.8 Ga Nagssugtoqidian Orogen, Southeastern Greenland: *Lithos*, doi: 10.1016/j.lithos.2017.10.017.
- Patchett, P. and Tatsumoto, M., 1980, Hafnium isotope variations in oceanic basalts: *Geophysical Research Letters*, v. 7, no. 12, p. 1077-1080, doi: 10.1029/GL007i012p01077.
- Paton, C., Woodhead, J. D., Hellstrom, J. C., Hergt, J. M., Greig, A. and Maas, R., 2010, Improved laser ablation U-Pb zircon geochronology through robust downhole fractionation correction: *Geochemistry, Geophysics, Geosystems*, v. 11, no. 3, doi: 10.1029/2009GC002618.
- Paton, C., Hellstrom, J., Paul, B., Woodhead, J. and Hergt, J., 2011, Iolite: Freeware for the visualisation and processing of mass spectrometric data: *Journal of Analytical Atomic Spectrometry*, v. 26, no. 12, p. 2508-2518, doi: 10.1039/C1JA10172B.
- Rayner, N., Stern, R. and Carr, S., 2005, Grain-scale variations in trace element composition of fluid-altered zircon, Acasta Gneiss Complex, northwestern Canada: *Contributions to Mineralogy and Petrology*, v. 148, no. 6, p. 721-734, doi: 10.1007/s00410-004-0633-8.
- Reimink, J., Davies, J., Chacko, T., Stern, R., Heaman, L., Sarkar, C., Schaltegger, U., Creaser, R. and Pearson, D., 2016, No evidence for Hadean continental crust within Earth's oldest evolved rock unit: *Nature Geoscience*, v. 9, no. 10, p. 777-780, doi: 10.1038/ngeo2786.
- Reimink, J. R., Chacko, T., Stern, R. A. and Heaman, L. M., 2014, Earth's earliest evolved crust generated in an Iceland-like setting: *Nature Geoscience*, v. 7, no. 7, p. 529-533, doi: 10.1038/ngeo2170.
- Russell, W. A., Papanastassiou, D. A. and Tombrello, T. A., 1978, Ca isotope fractionation on the Earth and other solar system materials: *Geochimica et Cosmochimica Acta*, v. 42, no. 8, p. 1075-1090, doi: 10.1016/0016-7037(78)90105-9.
- Salters, V. J., 1996, The generation of mid-ocean ridge basalts from the Hf and Nd isotope perspective: *Earth and Planetary Science Letters*, v. 141, no. 1-4, p. 109-123, doi: 10.1016/0012-821X(96)00070-2.
- Simonetti, A., Heaman, L. M., Hartlaub, R. P., Creaser, R. A., MacHattie, T. G. and Böhm, C., 2005, U-Pb zircon dating by laser ablation-MC-ICP-MS using a new multiple ion counting Faraday collector array: *Journal of Analytical Atomic Spectrometry*, v. 20, no. 8, p. 677-686, doi: 10.1039/B504465K.
- Sláma, J., Košler, J., Condon, D. J., Crowley, J. L., Gerdes, A., Hanchar, J. M., Horstwood, M. S. A., Morris, G. A., Nasdala, L., Norberg, N., Schaltegger, U., Schoene, B., Tubrett, M. N. and Whitehouse, M. J., 2008, Plešovice zircon — A new natural reference material for U-Pb and Hf isotopic microanalysis: *Chemical Geology*, v. 249, no. 1-2, p. 1-35, doi: 10.1016/j.chemgeo.2007.11.005.
- Stacey, J. S. and Kramers, J. D., 1975, Approximation of terrestrial lead isotope evolution by a two-stage model: *Earth and planetary science letters*, v. 26, no. 2, p. 207-221, doi: 10.1016/0012-821X(75)90088-6.
- Vervoort, J. D., Patchett, P. J., Blichert-Toft, J. and Albarède, F., 1999, Relationships between Lu-Hf and Sm-Nd isotopic systems in the global sedimentary system: *Earth and Planetary Science Letters*, v. 168, no. 1, p. 79-99, doi: 10.1016/S0012-821X(99)00047-3.
- Vezinet, A., Pearson, D. G., Thomassot, E., Stern, R. A., Sarkar, C., Luo, Y. and Fisher, C. M., 2018, Hydrothermally-altered mafic crust as source for early Earth TTG: Pb/Hf/O isotope and trace element

evidence in zircon derived from TTG of the Eoarchean Saglek Block, N. Labrador: *Earth and Planetary Science Letters*, v. 503, p. 95-107, doi: 10.1016/j.epsl.2018.09.015.

Wan, Y., Zhang, Y., Williams, I. S., Liu, D., Dong, C., Fan, R., Shi, Y. and Ma, M., 2013, Extreme zircon O isotopic compositions from 3.8 to 2.5Ga magmatic rocks from the Anshan area, North China Craton: *Chemical Geology*, v. 352, p. 108-124, doi: 10.1016/j.chemgeo.2013.06.009.

Wang, D., Guo, J.-h., Qian, Q. and Fu, B., 2018, Formation of late Archean high- $\delta^{18}\text{O}$  diorites through partial melting of hydrated metabasalts: *Journal of Petrology*, v. 59, no. 3, p. 419-446, doi: 10.1093/petrology/egy033.

Whitney, D. L. and Evans, B. W., 2010, Abbreviations for names of rock-forming minerals: *American mineralogist*, v. 95, no. 1, p. 185, doi: 10.2138/am.2010.337.

Woodhead, J., Hergt, J., Shelley, M., Eggins, S. and Kemp, R., 2004, Zircon Hf-isotope analysis with an excimer laser, depth profiling, ablation of complex geometries, and concomitant age estimation: *Chemical Geology*, v. 209, no. 1, p. 121-135, doi: 10.1016/j.chemgeo.2004.04.026.

Woodhead, J. D. and Hergt, J. M., 2005, A preliminary appraisal of seven natural zircon reference materials for in situ Hf isotope determination: *Geostandards and Geoanalytical Research*, v. 29, no. 2, p. 183-195, doi: 10.1111/j.1751-908X.2005.tb00891.x.

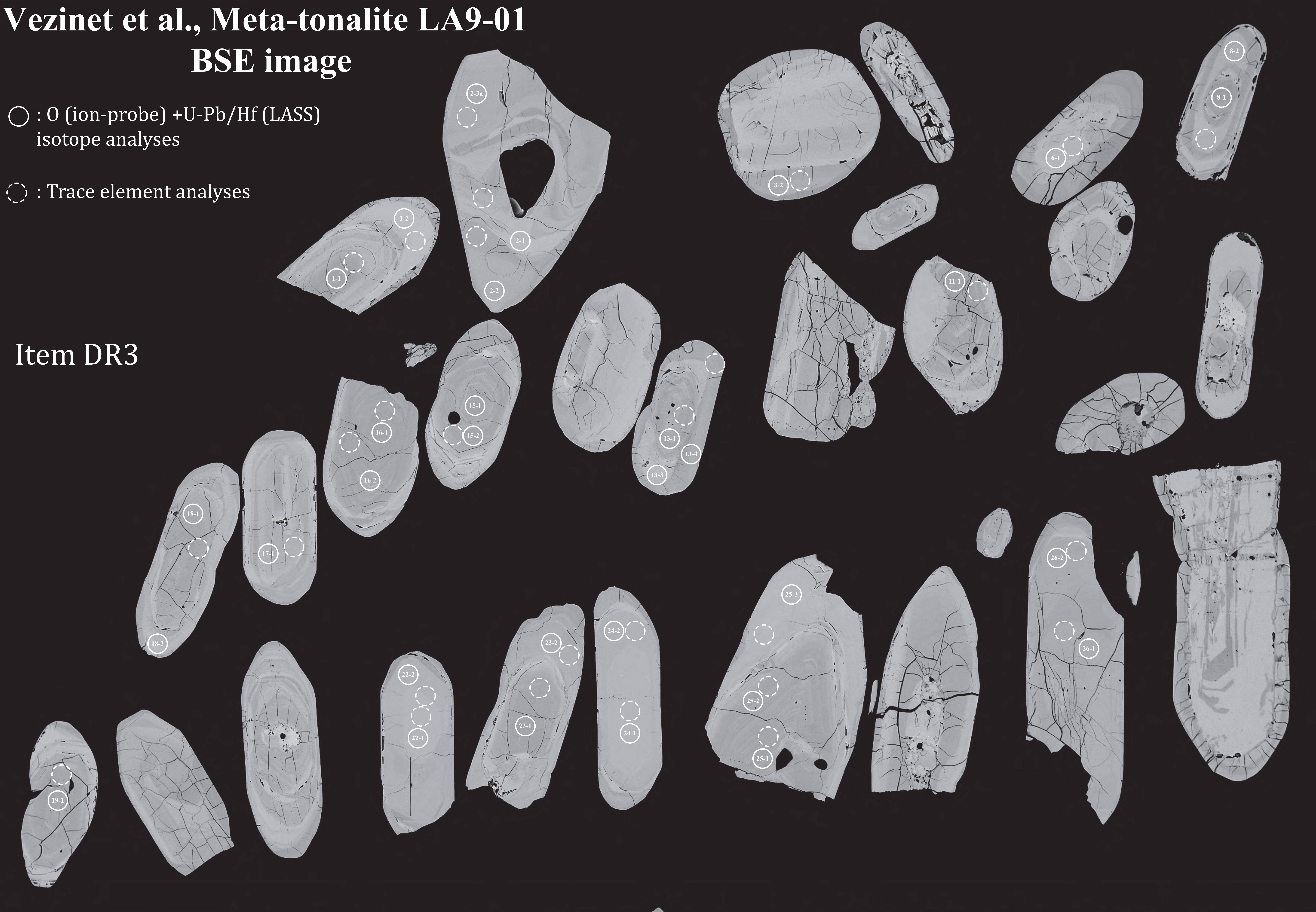


BSE image

○ : O (ion-probe) +U-Pb/Hf (LASS)  
isotope analyses

○ : Trace element analyses

Item DR3

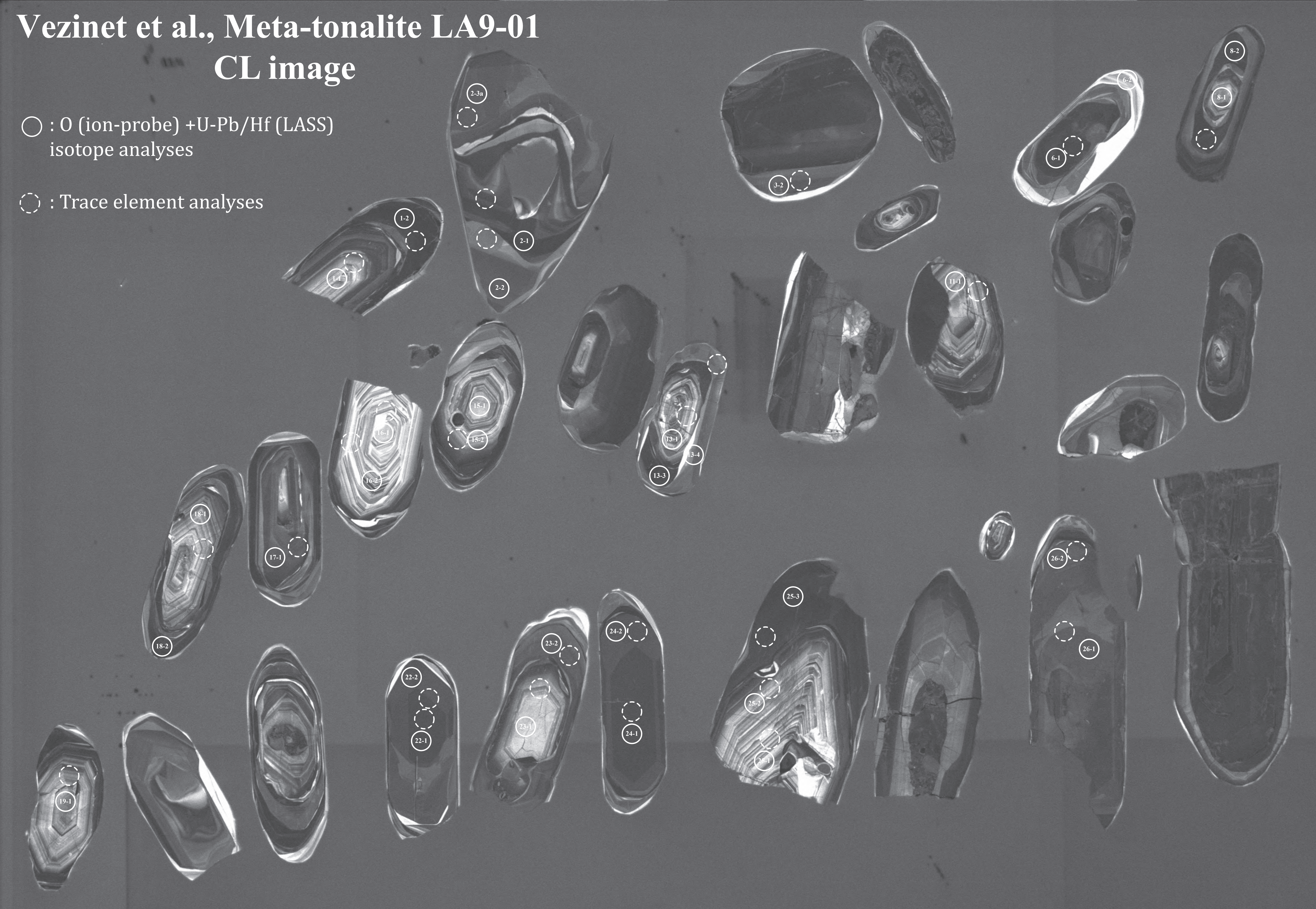


200  $\mu\text{m}^*$       Mag = 125 X      WD = 9.5 mm      Signal A = NTS BSD      EHT = 20.00 kV      Date :2 Feb 2018  
Specimen I = -3.69 nA      File Name = SEM18004\_M1483\_S5069B\_BS\_1.tif

CL image

○ : O (ion-probe) +U-Pb/Hf (LASS)  
isotope analyses

○ : Trace element analyses



100  $\mu\text{m}^*$       Mag = 124 X      WD = 15.0 mm      Signal A = Aux 1      EHT = 15.00 kV      Date :2 Feb 2018  
Specimen I = -3.66 nA      File Name = SEM18004\_M1483\_S5069B\_CL\_3.tif